**Optical measurement of endogenous ion channel voltage sensor activation in tissue**

Authors

Parashar Thapa[1‡], Robert Stewart[1‡], Rebecka J. Sepela[1], Oscar Vivas[2], Laxmi K. Parajuli[2], Mark Lillya[1], Sebastian Fletcher-Taylor[1], Bruce E. Cohen[3], Karen Zito[2], Jon T. Sack[1*]

[1]Department of Physiology and Membrane Biology, University of California, Davis, CA 95616

[2]Center for Neuroscience, University of California, Davis, CA 95616

[3]Molecular Foundry, Lawrence Berkeley National Laboratory, Berkeley, CA 94720

[‡]Authors contributed equally to this work

*Correspondence to jsack@ucdavis.edu

**Abstract**

A primary goal of molecular physiology is to understand how conformational changes of proteins affect the function of cells, tissues, and organisms. Here, we describe an imaging method for measuring the conformational changes of a voltage-sensing protein within tissue. We synthesized a fluorescent molecular probe, compatible with two-photon microscopy, that targets a resting conformation of Kv2-type voltage gated $K^+$ channel proteins. Voltage-response characteristics were used to calibrate a statistical thermodynamic model relating probe labeling intensity to the conformations adopted by unlabeled Kv2 proteins. Two-photon imaging of rat brain slices labeled with the probe revealed fluorescence consistent with conformation-selective labeling of endogenous neuronal Kv2 proteins. In principle, this method of quantifying endogenous protein conformational change from fluorescence images is generalizable to other proteins labeled with conformation-selective probes.

## Introduction

Proteins are dynamic, alternately settling into a few energetically favorable spatial arrangements, or conformations. Voltage-gated ion channels respond to changes in voltage across a cell membrane with conformational changes. These conformational changes are the initiating steps of a systemic physiological response to the voltage change.

Here, we describe an imaging method to measure conformational changes of voltage sensors of endogenous Kv2-type voltage-gated $K^+$ channels in tissue. Our objective in developing Kv2 imaging probes is to reveal conformational changes, with subcellular spatial resolution, which cannot be otherwise measured with conventional techniques. We have previously reported the synthesis and mechanistic validation of molecular probes that fluorescently label Kv2 voltage sensors in a conformation-sensitive fashion in heterologous cells (Tilley et al., 2014). We have now synthesized a probe specifically for fluorescence imaging in tissue, and developed an analysis method to quantify conformational changes of endogenous Kv2 channels. Quantification of Kv2 voltage sensor conformation in tissue will allow investigation of the effects of physiological events upon channels in their native environments, and enable novel measurements to assess how the coupling between voltage stimuli and channel conformational change are modulated by cells.

We engineered imaging probes of Kv2 channels to complement electrophysiological approaches conventionally used to measure channel activation. Recordings of ionic currents from voltage-clamped cell membranes has undergirded most mechanistic studies of $K^+$ channels, yet voltage-clamp preparations physically perturb the neuronal membranes studied, and have limited spatial resolution. Voltage clamp techniques are only effective in a limited number of reduced preparations where the electrical access resistance between electrodes and cell membrane is much less than the resistance of the cell membrane. In contrast, fluorescence imaging methods can have sub-micron spatial resolution and do not require electrical access nor mechanical disruption of tissue. Furthermore, the imaging method we have developed reports conformational changes distinct from ionic currents.

Kv2 channels serve physiological roles by conducting $K^+$ and also through their nonconducting functions. Kv2 channels are expressed in a wide variety of cell and tissue types throughout the bodies of vertebrates and invertebrates (Trimmer 1991, 2015, Patel *et al.* 1997, Yazulla & Studholme 1998, Schmalz *et al.* 1998, Amberg *et al.* 2004, Jacobson *et al.* 2007, Y. Zhang *et al.* 2008, Jegla *et al.* 2012, X. Li *et al.* 2015, Bocksteins 2016). Mammals form delayed-rectifier Kv2 channels from two Kv2 protein paralogs, Kv2.1 and Kv2.2, that combine as homo- or hetero-tetramers and can include auxiliary subunits (Kihira *et al.* 2010, Peltola *et al.* 2011, Bocksteins 2016, Bishop *et al.* 2018). Kv2 channels are critical for normal neurological function. In humans, *de novo* mutation of Kv2.1 channels leads to severe epilepsy and developmental delays (Torkamani *et al.* 2014, Saitsu *et al.* 2015, Thiffault *et al.* 2015, de Kovel *et al.* 2017).

In this study, we focus on Kv2 channels of rat brain neurons, where their physiological roles have been extensively studied. Kv2 channels are expressed in most central neurons and localize to cell bodies, proximal dendrites, and the axon initial segment (Trimmer 1991, Scannevin *et al.* 1996, Du *et al.* 1998, Murakoshi & Trimmer 1999, Lim *et al.* 2000, Kihira *et al.* 2010, King *et al.* 2014, Mandikian *et al.* 2014, Bishop *et al.* 2015, 2018). When Kv2 channels contribute to action potential repolarization, they modulate neuronal excitability (Du *et al.* 2000, Blaine & Ribera 2001, Liu & Bean 2014, Speca *et al.* 2014, Kimm *et al.* 2015, Hönigsperger *et al.* 2017, Palacio *et al.* 2017). However, in some neurons that have large Kv2 conductances, Kv2 channels open little, if at all during action potentials (Pathak *et al.* 2016, Y. Zheng *et al.* 2019). In addition to this variable coupling between action potentials and Kv2 opening, cells regulate the coupling between voltage stimuli and $K^+$ conduction of Kv2 channels by mechanisms including phosphorylation, oxidation, SUMOylation, and lipid metabolism (Misonou *et al.* 2004, 2005, Ramu *et al.* 2006, Y. Xu *et al.* 2008, Dai *et al.* 2009, Milescu *et al.* 2009, Plant *et al.* 2011, Cotella *et al.* 2012, Wu *et al.* 2013, Baver *et al.* 2014, Mandikian *et al.* 2014, Bishop *et al.* 2015). Furthermore, the majority of the Kv2.1 channels on the surface of rat hippocampal neurons have been proposed to be locked in a nonconducting state, from which the channels change conformation in response to voltage, yet are incapable of opening their $K^+$-conductive pore (O'Connell *et al.* 2010, Fox *et al.* 2013). It is not known whether voltage-sensitive conformational changes impact the established nonconducting functions of Kv2 proteins, such as regulating exocytosis and forming plasma membrane–endoplasmic reticulum junctions

(Antonucci *et al.* 2001, Feinshreiber *et al.* 2010, Fox *et al.* 2015, Fu *et al.* 2017, Johnson *et al.* 2018, Kirmiz, Palacio, *et al.* 2018, Kirmiz, Vierra, *et al.* 2018). As the coupling between voltage stimuli and the physiological outputs of Kv2 channels is variable, it is difficult to predict from protein localization alone what physiological roles voltage-sensing by Kv2 channels play in a cell.

The Kv2 probe we develop here measures conformational changes of Kv2 voltage sensor domains. Like other members of the voltage-gated cation channel superfamily, Kv2 channels contain specialized voltage sensor domains comprised of a bundle of four 'S1-S4' transmembrane helices (Long *et al.* 2005, 2007). The S4 helix contains positively charged arginine or lysine residues, 'gating charges', which respond to voltage changes by moving through the transmembrane electric field (Aggarwal & MacKinnon 1996, Seoh *et al.* 1996, Islas & Sigworth 1999). When voltage sensor domains encounter a transmembrane voltage that is more negative on the inside of the cell membrane, voltage sensors are biased towards 'resting' conformations, sometimes called down-states, in which gating charges are localized intracellularly. When voltage becomes more positive, gating charges translate towards the extracellular side of the membrane, and voltage sensors are progressively biased towards 'active' conformations, sometimes called up-states, in a process of 'voltage activation' (Armstrong & Bezanilla 1973, Zagotta *et al.* 1994, Tao *et al.* 2010, H. Xu *et al.* 2019). While activation of Kv2 voltage sensor domains does not guarantee pore opening (Scholle *et al.* 2004, Fox *et al.* 2013, Tilley *et al.* 2019), activation of voltage sensors are required for pore opening (Islas & Sigworth 1999). Thus, measuring whether Kv2 voltage sensors adopt resting *versus* active conformations determines whether a prerequisite for opening has occurred, and reveals the conformational state of nonconducting Kv2 proteins that may be coupled to other physiological outputs.

Conformational changes of voltage sensors have been detected with electrophysiological measurements of gating currents (Armstrong & Bezanilla 1973, M. F. Schneider & Chandler 1973, Bezanilla 2018) or by optical measurements from fluorophores covalently attached to voltage sensors by genetic encoding (Lin & Schnitzer 2016) and/or chemical engineering (G. Zhang *et al.* 2015). Each of these techniques have enabled breakthroughs in our understanding of how protein conformational changes are coupled to one another (J. Zheng & Trudeau 2016).

However, these existing techniques have limited utility for measuring voltage activation under physiological conditions: gating currents can only be measured when the proteins are expressed at high density in a voltage-clamped membrane, engineered channels differ from endogenous, and inserting fluorophores into voltage sensors irreversibly alters the structure and function of the labeled proteins. Here, we develop a different strategy, where fluorescent probes dynamically label endogenous voltage sensors to reveal conformational states.

The fluorescent Kv2 probe we developed is a synthetic derivative of the tarantula peptide guangxitoxin-1E (GxTX). GxTX is an allosteric inhibitor selective for Kv2 (Herrington *et al.* 2006, Milescu *et al.* 2009, Schmalhofer *et al.* 2009, Liu & Bean 2014, Gupta *et al.* 2015). GxTX has a high affinity for resting voltage sensors: 13 nM for rat Kv2.1 in CHO-K1 cells (Tilley *et al.* 2014) . When Kv2.1 voltage sensors adopt active conformations, GxTX affinity becomes at least 5400-fold weaker (Tilley *et al.* 2019). Fluorescently-tagged derivatives of GxTX label cell surfaces where Kv2.1 proteins are heterologously expressed. When voltage sensors adopt active conformations, GxTX dissociates from the cell surface and diffuses into the extracellular solution (Tilley *et al.* 2014). Our goal is to exploit the conformation-selective binding of a GxTX-based probe to measure where and when Kv2 proteins adopt resting *versus* active conformations in tissue. To do this, we synthesized GxTX-594, a molecular probe compatible with two-photon imaging through light scattering tissue. We determined that the fluorescence from this probe accurately reports the conformational state of Kv2 channels in heterologous cells. Crucially, we also developed a method to quantify the degree of Kv2 voltage sensor conformational change from images of GxTX-594 fluorescence. We then deployed the GxTX-based probe for two-photon imaging in brain slices and identified voltage-sensitive fluorescence changes that indicate conformational changes of endogenous neuronal Kv2 channels.

## Results

Throughout this study, we refer to molecules designed to report conformational changes of ion channels as Endogenous Channel Activity Probes or ECAPs. We previously presented an ECAP that was a synthetic derivative of the tarantula peptide guangxitoxin-1E (GxTX) conjugated to a DyLight 550 fluorophore (GxTX-550) (Tilley *et al.* 2014). DyLight 550 has poor two-photon excitation properties, and for this study it was replaced with a fluorophore that has more desirable photophysical properties. Alexa 594 exhibits a large two-photon excitation cross-section and ample spectral separation from green fluorescent protein (GFP), making it well-suited for multiplexed, two-photon experiments (Bestvater *et al.* 2002). We chemoselectively conjugated Alexa 594-maleimide to a synthetic GxTX Ser13Cys derivative to create the ECAP used throughout this study, GxTX-594 (Fig 1 Supplement 1).

### *GxTX-594 colocalizes with Kv2.1 and Kv2.2, but not other $K^+$ channels*

To determine whether this ECAP could potentially identify activation of Kv2 channels in tissue, we first characterized its selectivity for Kv2 channels over other channels, each heterologously expressed in isolation. We conducted multiplex imaging of GxTX-594 and GFP-tagged $K^+$ channel subunits to assess colocalization. $K^+$ channels were expressed in the CHO-K1 cell line, which has been found to not harbor endogenous $K^+$ currents (Gamper *et al.* 2005). We first assessed whether GxTX-594 binds Kv2 channels. Mammals have two Kv2 pore-forming subunits, Kv2.1 and Kv2.2, both of which are expressed in neurons throughout the brain (Trimmer 1991, Kihira *et al.* 2010, Bishop *et al.* 2015). CHO cells were transfected with either a rat Kv2.1-GFP or Kv2.2-GFP construct and were imaged 2 days later. Both Kv2.1-GFP and Kv2.2-GFP transfections yielded delayed rectifier $K^+$ currents (Fig 2, Supplement 1 A). Kv2.1-GFP and Kv2.2-GFP fluorescence appeared at the apparent surface membrane of the CHO cells, and the fluorescence was localized predominantly to the glass-adhered basal surface, where it adopted a clustered morphology (Fig 1 A). Clustered basal expression is a hallmark of Kv2 channel localization in neurons and other mammalian cells when they are adhered to glass (Shi *et al.* 1994, Antonucci *et al.* 2001). In cultured HEK293 cells, COS-1 cells, and central neurons, clusters mark cortical endoplasmic reticulum junctions with the plasma membrane (Antonucci *et al.* 2001, Fox *et al.* 2015, Cobb *et al.* 2016, Johnson *et al.* 2018, Kirmiz, Palacio, *et al.* 2018, Kirmiz, Vierra, *et al.* 2018). After incubation with membrane-impermeant GxTX-594 (100 nM

for 5 minutes), fluorescence localized to regions with Kv2-GFP signal (Fig 1 A). GxTX-594, and Kv2.1-GFP or Kv2.2-GFP, had Pearson correlation coefficients that averaged 0.86 or 0.80, respectively, verifying a high degree of colocalization of both Kv2 proteins with GxTX-594 (Fig 1 B). The ratio of GxTX-594 to GFP fluorescence intensity was similar for Kv2.1-GFP or Kv2.2-GFP (Fig 1 B), consistent with the lack of discrimination of GxTX between Kv2.1 and Kv2.2 (Herrington *et al.* 2006).

To test whether GxTX-594 binds other subtypes of $K^+$ channels, we quantified labeling of cells expressing other GFP-labeled $K^+$ channel subtypes. Electrophysiological studies have concluded that the native GxTX peptide is selective for Kv2 channels, with some off-target modulation of A-type Kv4 current (Herrington *et al.* 2006, Liu & Bean 2014, Speca *et al.* 2014) . However, electrophysiological testing only indicates whether GxTX modulates channels; electrophysiology cannot detect ligands that bind channels, but do not alter currents (Sack *et al.* 2013). Furthermore, structural differences between wild-type GxTX and the GxTX-594 variant could potentially alter selectivity among channel subtypes. GFP-$K^+$ channel fusions were selected that express and retain function with a GFP tag: rat Kv4.2-GFP (Shibata *et al.* 2003), rat Kv1.5-GFP (H. Li *et al.* 2001), and mouse BK-GFP. Transfection of each of these channel subtypes into CHO cells resulted in voltage-dependent outward currents, consistent with cell surface expression of the $K^+$ channels (Fig 2, Supplement 1A). As the other $K^+$ channels did not preferentially localize to the basal membrane as did Kv2.1 and Kv2.2, imaging planes above the basal surface were chosen for consistency. A fluorescent wheat germ agglutinin (WGA) conjugate was used to identify the membrane surface. After incubation with 100 nM GxTX-594 for five minutes, cells expressing Kv4.2, Kv1.5, or BK channels were not appreciably labeled by GxTX-594 (Fig 2, Supplement 1 B). When the background-subtracted GxTX-594:GFP fluorescence intensity ratio was normalized to GxTX-594:Kv2.1-GFP, this ratio was close to zero for Kv4.2, Kv1.5, or BK (Fig 2, Supplement 1 C), suggesting minimal binding to these channel subtypes. Furthermore, no colocalization was apparent between Kv4.2, Kv1.5, or BK and GxTX-594 (Fig 2 Supplement 1 D). However, we noticed that in these experiments the majority of GFP signal from Kv4.2 and Kv1.5 channels did not colocalize with the WGA cell surface marker, suggesting the majority of channels were retained intracellularly (Fig 2, Supplement 1 B). More efficient cell surface expression was achieved by co-transfection with

auxiliary subunits: Kv4.2 with KChIP2 (Shibata *et al.* 2003) and Kv1.5 with Kvβ2 (Shi *et al.* 1996). The experiments were repeated, with airydisk imaging for improved resolution (Fig 2 A). Similarly, GxTX-594 fluorescence was not apparent on cells expressing Kv4.2 + KChIP2, Kv1.5 + Kvβ2, or BK (Fig 2 B and C). While not a complete survey of all the 80 voltage-gated ion channels in the mammalian genome, these results indicate that GxTX-594 fluorescence selectively labels cell surfaces where Kv2.1 or Kv2.2, but not other $K^+$ channels are expressed.

***GxTX-594 binds Kv2.1 in the presence of its neuronal auxiliary subunit AMIGO-1***

AMIGO-1 is an auxiliary subunit for Kv2 channels, that is colocalized with Kv2 channels in most if not all neurons the brain (Bishop *et al.* 2018). AMIGO-1 is a single-pass transmembrane protein with a large extracellular domain, an architecture similar to auxiliary subunits of voltage-gated sodium channels, Kv4 channels, or BK channels that modulate binding of peptide toxins to voltage-gated ion channels (Xia *et al.* 1999, Gilchrist *et al.* 2013, Maffie *et al.* 2013). To determine if AMIGO-1 affects GxTX-594 channel labeling, Kv2.1-expressing cells were transiently transfected with an AMIGO-1-YFP construct and assayed for GxTX-594 binding. For these experiments, Kv2.1 channels were expressed in a CHO-K1 cell line stably transfected with rat Kv2.1 under control of a tetracycline-inducible promoter (Kv2.1-CHO) (Trapani & Korn 2003). Consistent with Kv2.1:AMIGO-1 colocalization observed in other cell types (Peltola *et al.* 2011, Bishop *et al.* 2018), AMIGO-1-YFP fluorescence was observed in clusters at the basal membrane (Fig 3 A) similar to Kv2.1-GFP (Fig 1 A). GxTX-594 labeled both AMIGO-1 positive and AMIGO-1 negative cells (Fig 3 A). Pearson's correlation coefficients indicated colocalization between AMIGO-1 and GxTX-594, consistent with AMIGO-1 colocalizing with clustered Kv2.1 (Fig 3 B). Increasing concentrations of GxTX-594 were applied to the cells and the relationship between GxTX-594 fluorescence intensity and dose was quantified for AMIGO-1 positive and negative cells (Fig 3 C). A Langmuir binding isotherm was fit to GxTX-594 fluorescence intensity (lines, Fig 3 D), and resulted in an indistinguishable dissociation constant between AMIGO-1 positive (27 ± 14 nM) and AMIGO-1 negative cells (26.9 ± 8.3 nM), thus there was no indication that AMIGO-1 disrupted the GxTX-594–Kv2 interaction.

***GxTX-594 fluorescence dynamics report Kv2 channel voltage activation***

To understand the relationship between channel gating and GxTX-594 fluorescence, we determined how fluorescence intensity on cells expressing Kv2.1 responded to changes in voltage. For these experiments, Kv2.1-CHO cells were incubated for 5 minutes in a bath solution containing 100 nM GxTX-594 before dilution with extracellular solution to 9 nM, and imaged at least 9 minutes after dilution. Fluorescence intensity images were generated from airy disk confocal imaging of cells voltage-clamped in the whole-cell patch clamp configuration. Cells were held at -80 mV and stepped to test potentials while measuring fluorescence (Fig 4 A). A region of interest (ROI) corresponding to the cell surface was manually identified and average fluorescence intensity quantified from time lapse sequences. Average fluorescence intensity from the cell surface was background-subtracted using the average fluorescence intensity from an ROI in a region without cells. Both the amplitude and kinetics of fluorescence change from cell surface ROIs were sensitive to voltage (Fig 4 B), similar to prior findings with GxTX-550 (Tilley *et al.* 2014). This suggests the mechanism underlying the voltage-dependent fluorescence change of GxTX-594 is similar to GxTX-550: a conformational change in the voltage sensor of Kv2.1 causes a change in affinity for GxTX-594, binding or unbinding causes GxTX-594 to enter or leave imaging voxels containing Kv2.1, and this redistribution of GxTX-594 is responsible for the dynamic fluorescent labeling or unlabeling of the cell surfaces. Additionally, cells appeared to approach a baseline fluorescence intensity above background even when given a +80 mV depolarizing voltage stimulus (Fig 4 B). This residual fluorescence varied between cells (Fig 4 C) and was potentially due to internalized GxTX-594 and/or autofluorescence. However, some residual fluorescence appeared to be localized to the cell surface membrane (Fig 4 A). As such membrane labeling was absent in the absence of Kv2 channels (Fig 2), this fluorescence could indicate a population of Kv2.1 channels that reside at the cell surface and bind GxTX-594 in a fashion that renders the Kv2.1–GxTX complex insensitive to voltage.

We conducted experiments to determine which region of voltage-clamped cells to quantitate dynamic fluorescence from. The confocal imaging plane containing the most GxTX-594 fluorescence was the glass-adhered basal surface. We noticed that GxTX-594 fluorescence in the center of the basal surface appeared to respond more slowly to voltage than the periphery. To quantify this observation, ROIs were drawn in the center of the basal surface of the cell and its

average fluorescence intensity was compared to an ROI at the cell periphery. In response to voltage change, the kinetics of fluorescence change were slower at the center of the basal surface and faster towards the outer periphery (Fig 4 Supplement 1 A and B). We quantified rates of fluorescence change ($k_{\Delta F}$) by fitting a monoexponential function:

$$F = F_{\infty} + F_0 e^{\frac{(t-t_0)}{\tau}} \quad \text{(Equation 1)}$$

Where $\tau = k_{\Delta F}$, $t$ = time, $t_0$ = time at start of fit, $F$ = fluorescence intensity, $F_0$ = fluorescence at start of fit, $F_{\infty}$ = fluorescence after infinite time. $k_{\Delta F}$ progressively slowed as the ROI contracted from the perimeter of the cell (Fig 4 Supplement 1 C and D). This difference in kinetics suggests that the concentration of freely diffusing GxTX-594 in the restricted space between the cell membrane and the glass surface is transiently non-uniform after voltage change. The location dependence of $k_{\Delta F}$ was more pronounced during GxTX-594 labeling at -80 mV (Fig 4 Supplement 1 D) than unlabeling at +40 mV (Fig 4 Supplement 1 C). We suspect that the more extreme location dependence at -80 mV is due to a high density of Kv2.1 binding sites in the restricted extracellular space between the cell membrane and glass coverslip, such that GxTX-594 is depleted from solution by binding Kv2.1 before reaching the center of the cell. After unbinding at +40 mV, each GxTX-594 molecule is less likely to rebind to Kv2.1 as it diffuses out from under the cell, because Kv2.1 voltage sensors are in an active, low affinity conformation (Tilley *et al.* 2014, 2019). This expected difference in GxTX-594 buffering by Kv2.1 could explain the difference in location dependence of $k_{\Delta F}$ during labeling at -80 mV and unlabeling at +40 mV. To avoid complications resulting from the variability of kinetics at the basal surface, further voltage-dependent labeling experiments were conducted while imaging at a plane above the coverslip, where the cell surface has unrestricted access to the extracellular solution (Fig 4 A).

We next determined the range of voltages that triggered dynamic labeling of Kv2.1 by GxTX-594. We quantified labeling intensity between cells by normalizing initial fluorescence at a holding potential of -80 mV to be 100% $F/F_{init}$ and residual fluorescence after a +80 mV step to be 0% $F/F_{init}$ (Fig 4 D). The fluorescence–voltage response was fit with a Boltzmann function with a half maximal voltage midpoint ($V_{1/2}$) of -27 mV and a steepness ($z$) of 1.4 elementary charges ($e_0$) (Fig 4 C, black line). This is strikingly similar to the voltage dependence of integrated gating charge from Kv2.1-CHO cells, without any GxTX present $V_{1/2}$ = -26 mV, $z$ =

1.6 $e_0$ (Tilley *et al.* 2019). The similarity suggests that the degree of GxTX-594 labeling corresponds to the fraction of the channels' voltage sensors that have their gating charges in their most intracellular resting conformation. Although GxTX-based probes perturb the gating of the Kv2.1 channels they label, under these conditions the voltage dependence of GxTX-594 labeling is similar to the voltage dependence of the resting conformation of unlabeled Kv2.1 channels (discussed further below).

To determine the temporal response of GxTX-594 labeling to voltage change, we compared $k_{\Delta F}$ response to varying step potentials (Fig 4 E). In response to voltage steps from a holding potential of -80 mV to more positive potentials, $k_{\Delta F}$ increased progressively from approximately -40 mV to +40 mV. After a return to -80 mV, labeling occurred at a rate similar to unlabeling at -40 mV, indicating that the rate of relaxation to a labeled/unlabeled equilibrium saturates below -40 mV. A saturation of the temporal response characteristics was also observed with the GxTX-550 probe (Tilley *et al.* 2014). The $k_{\Delta F}$–voltage response was fit with a Boltzmann (Eq. 2) resulting in $V_{1/2}$ = +2 mV and $z$ = 1.1 $e_0$ (Fig 4 E, black line). Notably, the dynamic fluorescence responses of GxTX-594 to voltage changes occurred at physiologically relevant potentials, suggesting that changes in GxTX-594 labeling intensity or rate could occur in response to changes in cellular electrical signaling.

There was substantial variability in $k_{\Delta F}$ between cells (Fig 4 E). We wondered if this could be due to fluctuations in ambient temperature (27-29°C), given the substantial temperature sensitivity reported for Kv2.1 conductance (F. Yang & Zheng 2014). To assess the temperature dependence of GxTX-594 labeling, the cell bath solution was heated to either 27°C or 37°C and stepped to 0 mV for a measurement of $k_{\Delta F}$ (Fig 4 Supplement 2). The fold change in $k_{\Delta F}$ over this 10 °C difference, or $Q_{10}$, was 3.8-fold. This was less than the up to 6-fold cell-to-cell variability observed under otherwise identical conditions. This indicates that the variation in $k_{\Delta F}$ is likely not attributed to temperature variation, and suggests that there are determinants of $k_{\Delta F}$ variability which are intrinsic to individual cells.

***The relation between voltage sensor activation and fluorescence dynamics can be recapitulated by rate theory modeling.***

To enable translation of fluorescence intensity of GxTX-594 into a measure of channel conformational change, we developed a general model relating ECAP labeling to voltage sensor activation. In this model, the ratio of labeled to unlabeled Kv2 is determined by binding and unbinding rates of the ECAP (Scheme I).

**Scheme I**

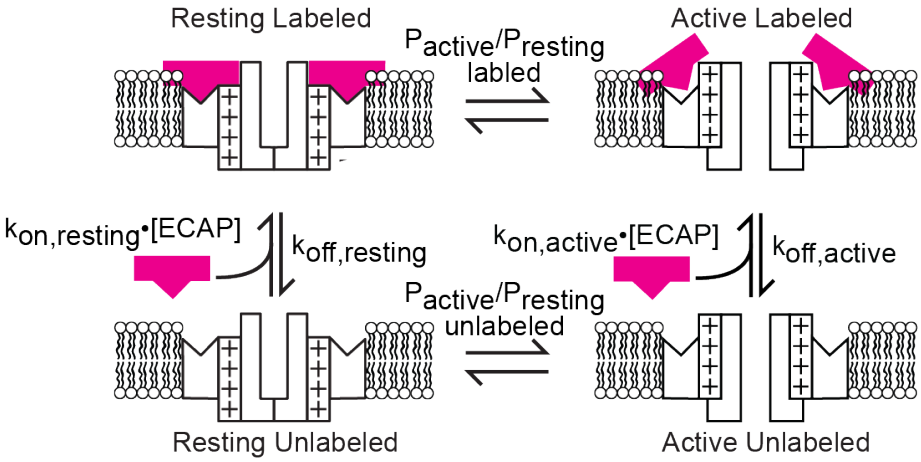


**Scheme II**

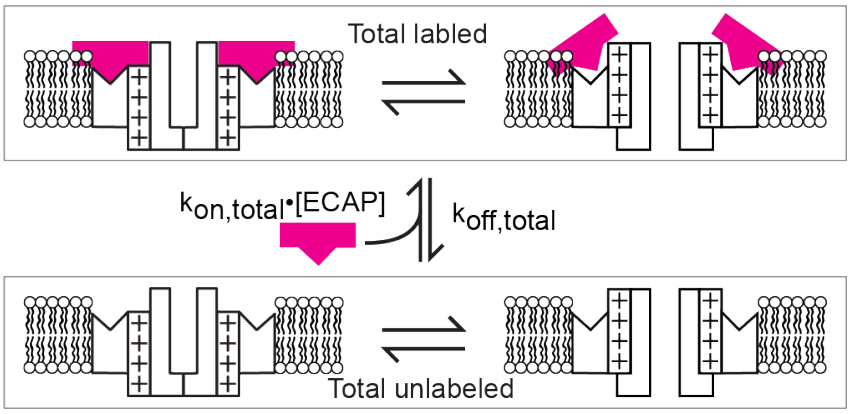


The Scheme I model assumes the innate voltage sensitivity of the Kv2 channel is solely responsible for controlling voltage dependence. Labeling is voltage-dependent because the binding and unbinding rates are different for resting and active conformations of voltage sensors. When voltage sensors change from resting to active conformations, the binding rate of an ECAP decreases and the unbinding rate increases. When the membrane voltage is held constant for sufficient time, the proportions of labeled and unlabeled channels reach an equilibrium. Scheme I assumes that voltage sensor conformational changes equilibrate much faster than ECAP binding

or unbinding, such that binding and unbinding are the rate-limiting steps. As ECAP labeling requires seconds to equilibrate (Fig 4 E), and Kv2 channel gating equilibrates in milliseconds (Tilley *et al.* 2019), about 3 orders of magnitude more quickly, the simplifying approximation that voltage sensor conformations are in continuous equilibrium appears reasonable. Kv2 channels couple many conformational changes to each other and their gating is more complex than a single voltage sensor conformational change (Scholle *et al.* 2004, Jara-Oseguera *et al.* 2011, Tilley *et al.* 2019). However, models which presume independent activation of a voltage sensor in each of the four Kv2.1 subunits accurately predict many aspects of voltage activation and voltage sensor toxin binding (Lee *et al.* 2003, Tilley *et al.* 2019). Thus, we found it reasonable to model voltage sensor activation of Kv2 channels as a single, rapid transition of each voltage sensor from a resting conformation, to an active conformation. With this model, at any given voltage, there is a probability that a voltage sensor is either in its resting conformation ($P_{resting}$), or in its active conformation ($P_{active}$), such that $P_{active} = (1 - P_{resting})$. The equilibrium for voltage sensor activation is then a ratio of active to resting voltage sensors ($P_{active}/P_{resting}$) in which

$$\frac{P_{active}}{P_{resting}} unlabeled = e^{(V - V_{1/2,unlabeled})\frac{zF}{RT}} \qquad \text{Equation 2a}$$

$$\frac{P_{active}}{P_{resting}} labeled = e^{(V - V_{1/2,labeled})\frac{zF}{RT}} \qquad \text{Equation 2b}$$

where $V_{1/2}$ is the voltage where $P_{active}/P_{resting,} = 1$, $z$ is the number of elementary charges determining voltage dependence, $F$ is the Faraday constant, $R$ is the ideal gas constant, and $T$ is absolute temperature. In a prior study, we fit the gating charge–voltage relation of Kv2.1 with a Boltzmann distribution that yielded $V_{1/2}$ = -31.7 mV with $z = 1.5\ e_0$, and found that with a saturating concentration of GxTX $V_{1/2}$ = 41.3 mV (Tilley *et al.* 2019). These values were used for $V_{1/2,unlabled}$, $z$, *and* $V_{1/2,unlabled}$ respectively (Table 1). To relate voltage sensor activation to labeling and unlabeling, we used microscopic binding ($k_{on}[ECAP]$) and unbinding ($k_{off}$) rates that are distinct for resting and active voltage sensors. We estimated values for these rates assuming

$$k_{\Delta F} = k_{on}[ECAP] + k_{off} \qquad \text{(Equation 3)}$$

and

$$K_d = \frac{k_{off}}{k_{on}} \qquad \text{(Equation 4)}$$

In 9 nM GxTX-594, the Boltzmann fit of the $k_{\Delta F}$–voltage relation saturates at negative voltages with $k_{\Delta F}$ = 7.6 x $10^{-3}$ $s^{-1}$ (Fig 4 E). We used that value and $K_d$ = 27 nM from GxTX-594 labeling of CHO cells (Fig 3 D), to calculate the $k_{on,resting}$ and $k_{off,resting}$ values in Table 1. In 9 nM GxTX-594, at greater than +40 mV, voltage-dependent unlabeling was nearly complete, indicating that $k_{off,active} >> k_{on,active}[ECAP]$. We used the saturation of $k_{\Delta F}$ = 0.31 $s^{-1}$ at positive voltages to calculate $k_{off,active}$ (Fig 4 E). As slow labeling of active voltage sensors was expected to confound measurement of $k_{on,active}$, we used the statistical thermodynamic principle of microscopic reversibility (Lewis 1925) to constrain $k_{on,active}$:

$$\frac{\frac{P_{active}}{P_{resting}}, labeled}{\frac{P_{active}}{P_{resting}}, unlabeled} = \frac{\frac{k_{off,resting}}{k_{on,resting}}}{\frac{k_{off,active}}{k_{on,active}}} \qquad \text{(Equation 5)}$$

At any static voltage, the simplifying assumption that voltage sensors are in continuous equilibrium allows Scheme I to collapse into Scheme II, which has only a single microscopic binding rate, $k_{on,total}[ECAP]$, and unbinding rate, $k_{off,total}$. In Scheme II, $k_{on,total}$ is a weighted sum of both $k_{on,resting}$ and $k_{on,active}$ from Scheme I. The weights for $k_{on,total}$ are the relative probabilities that unlabeled voltage sensors are resting or active, which is determined by the Boltzmann distribution at a specified voltage ($\frac{P_{active}}{P_{resting}} labeled$):

$$k_{on,total} = k_{on,resting}[ECAP] \cdot \frac{1}{1+\frac{P_{active}}{P_{resting}} unlabeled} + k_{on,active}[ECAP] \cdot \frac{1}{1+\frac{1}{\frac{P_{active}}{P_{resting}} unlabeled}}$$

(Equation 6)

Similarly, $k_{off,total}$ is determined by the unbinding rate from resting voltage sensors ($k_{off,resting}$) and the unbinding rate from active voltage sensors ($k_{off,active}$), and weighted such that:

$$k_{off,total} = k_{off,resting} \cdot \frac{1}{1+\frac{P_{active}}{P_{resting}} labeled} + k_{off,active} \cdot \frac{1}{1+\frac{1}{\frac{P_{active}}{P_{resting}} labeled}} \qquad \text{(Equation 7)}$$

Using $k_{on,total}$ and $k_{off,total}$ we can compute $k_{\Delta F}$ using Equation 3. To test the predictive value of the Scheme II model, we compared the predicted $k_{\Delta F}$ to experimental measurements in 9 nM GxTX-594 (Fig 4 E, blue line). This reasonably reproduced the voltage dependence of Kv2.1 labeling.

The Scheme II model was also used to predict the magnitude of ECAP fluorescence changes on cell surfaces. The fluorescence at equilibrium at any voltage ($F_\infty$) relative to fluorescence at another voltage ($F_0$) is the probability at equilibrium that a Kv2 subunit is labeled by the ECAP ($P_{labeled}$) at the initial and final voltages:

$$\frac{F_\infty}{F_0} = \frac{P_{labeled,final\ voltage}}{P_{labeled,initial\ voltage}} \qquad \text{(Equation 8)}$$

The $P_{labeled}$ at equilibrium at any voltage can be determined from microscopic binding rates associated with Scheme II where:

$$P_{labeled} = \frac{1}{1+\frac{K_{d,total}}{[ECAP]}} = \frac{1}{1+\frac{k_{off,total}}{k_{on,total}\cdot[ECAP]}} \qquad \text{(Equation 9)}$$

Using our model, we calculated the fluorescence–voltage relation from $P_{labeled}$ (Equation 8) and compared these calculated values to our experimental data. The model predicts fluorescence response within the range of the experimental data (Fig 4 D, blue line).

The Scheme II model relating labeling to voltage sensor activation was developed for static voltages. However, in electrically active cells, voltage is dynamic. In neurons, action potentials involving Kv2 currents occur on the millisecond time scale (Liu & Bean 2014, Kimm *et al.* 2015), orders of magnitude faster than the GxTX-594 response. The Scheme II model assumes that voltage sensors are in continuous equilibrium, and this assumption breaks down when voltage is rapidly changing, as Kv2 voltage sensor movements with or without GxTX require milliseconds to equilibrate (Tilley *et al.* 2019). Thus, the slow ECAP response will integrate voltage fluctuations occurring over many seconds. We determined whether the model could predict GxTX-594 labeling in response to action potential-like voltage changes by stimulating voltage-clamped Kv2.1-CHO cells with brief voltage steps that crudely mimic action potentials.

We stimulated with trains of 2 ms voltage steps from -80 to +40 mV, and observed a change in cell surface fluorescence (Fig 5 A, B). To assess frequency response, step frequency was varied from 0.02 to 200 Hz. At frequencies higher than 25 Hz, detectable unlabeling occurred (Fig 5 C). Similar to the voltage dependence of this ECAP, $k_{\Delta F}$ varied with stimulus frequency (Fig 5 D).

Frequency-dependent predictions of $F/F_{init}$ and $k_{\Delta F}$ were made from the Scheme II model. These predictions were calculated assuming the summed probability of being at each voltage (-80 or +40 mV) determines the overall $P_{labeled}$ (Equations 10 and 11).

$$k_{\Delta FHz} = (P_{40mV} \cdot k_{\Delta F40mV}) + (P_{-80mV} \cdot k_{\Delta F-80mV}) \qquad \text{(Equation 10)}$$

$$\mathrm{F}/F_{init} = (P_{40mV} \cdot \Delta F_{40mV}) + (P_{-80mV} \cdot \Delta F_{-80mV}) \qquad \text{(Equation 11)}$$

The predicted frequency responses of the Scheme II model did not perfectly match empirical measurements. The model produced a frequency dependence of $k_{\Delta F}$ that was within the range of the empirical data (Fig 5 D, blue line). The model required higher stimulus frequencies to produce the changes in fluorescence intensity observed empirically (Fig 5 C, blue line). This discrepancy could be due to Kv2.1 voltage sensors having insufficient time to equilibrate at high stimulus frequencies: at -80 mV the time constant of gating current decay from Kv2.1-CHO cells was 22 ms. However, the slopes of the model and the empirical frequency responses appeared similar. The similarity of slope was assessed by fitting the empirical data with a Boltzmann distribution assuming a conformational equilibrium determined by $P_{40mV}/P_{-80mV}$ (Fig 5 C, black line). The coincidence of the empirical and theoretical slopes is striking, and suggests that the Scheme II model of ECAP labeling has some predictive power even when voltage varies faster than ion channel voltage sensors can respond.

***Labeling intensity is proportional to overall voltage sensor activation***

We used the ECAP model to investigate general principles of the relation between voltage sensor activation and labeling. In particular, we were interested in exploiting ECAP labeling to reveal information about voltage sensor activation in the unlabeled channel population. The model predicts that when an ECAP is applied at sub-saturating concentrations (below the $K_d$ for resting

voltage sensors), the change in labeling is proportional to the probability of unlabeled voltage sensors becoming active (Fig 6 A). This, perhaps counterintuitive, phenomenon emerges when the majority of voltage sensors are unlabeled, and this unlabeled majority dominates the response of the overall population. The lower the concentration of the ECAP, the more closely its labeling response matches the voltage sensor activation of unlabeled channels. This model predicts that the degree of unlabeling with 9 nM GxTX-594 (Fig 4 D), is nearly proportional to the degree of voltage sensor activation. Thus, a broad qualitative conclusion can be made from ECAP fluorescence changes: a change in labeling indicates that voltage sensors of unlabeled channels have changed their probability of being in active conformations.

***Labeling/unlabeling kinetics are concentration-insensitive at sub-saturating concentrations***

The ECAP model predicts the observed changes in the $k_{\Delta F}$ for GxTX-594 (Fig 4 E). The voltage dependence of $k_{\Delta F}$ appears to saturate at extreme positive and negative voltages, and the model provides some insight into the thermodynamics underlying these responses. At extreme positive voltages, $k_{\Delta F}$ is almost exclusively determined by labeling and unlabeling of active voltage sensors. Similarly, at negative voltages, $k_{\Delta F}$ is determined by labeling and unlabeling of resting voltage sensors. Interestingly, as the concentration drops below the $K_d$ of resting voltage sensors, $k_{\Delta F}$ becomes insensitive to the concentration of ECAP (Fig 6 B) because the kinetics are determined primarily by $k_{off}$ (Equation 3,7). Thus, all subsaturating concentrations of ECAPs are expected to produce similar $k_{\Delta F}$ responses. This indicates that if the concentration of ECAP applied to a tissue is below the $K_d$, the fluorescence kinetics are expected to be consistent throughout a tissue, and insensitive to vagaries in ECAP concentration.

***GxTX-594 labels Kv2 channels in brain slices***

Having determined that GxTX-594 indicates the location of Kv2 channels and developed a methodology to convert fluorescence changes into a measure of voltage sensor activation, we proceeded to assess the potential of GxTX-594 as an ECAP to report Kv2 activation in living tissue. We looked in rat brain at CA1 pyramidal neurons of the hippocampus, as the physiology of these neurons have been intensively studied, their electrical properties are relatively homogeneous, and they express Kv2 channels (Misonou *et al.* 2005) .

To test whether GxTX-594 can identify Kv2 channel location in neurons, we assessed its colocalization with overexpressed Kv2.1-GFP. Organotypic hippocampal slice cultures prepared from postnatal day 5-7 rats were sparsely transfected with Kv2.1-GFP, resulting in a subset of neurons displaying green fluorescence. When imaged two to four days after transfection, GFP fluorescence was seen evenly dispersed throughout the plasma membrane surrounding neuronal cell bodies and proximal dendrites (Fig 7 Supplement 1 A and B). Six days or more after transfection, Kv2.1-GFP fluorescence organized into clusters on the cell soma and proximal processes (Fig 7, Fig 7 Supplement 1 C), a pattern consistent with a prior report of endogenous Kv2.1 in CA1 neurons (Misonou *et al.* 2005). After identifying a neuron expressing Kv2.1-GFP, solution flow into the slice bath was stopped and GxTX-594 was added to the static bath solution to a final concentration of 100 nM. After five minutes of incubation, solution flow was restarted, leading to wash-out of GxTX-594 from the slice bath. After wash-out, GxTX-594 fluorescence remained colocalized with Kv2.1-GFP (Fig 7, Fig 7 Supplement 1), indicating that GxTX-594 is able to permeate through dense neural tissue and bind to Kv2 channels on neuronal surfaces. Pearson correlation coefficients confirmed the colocalization of GxTX-594 with Kv2.1-GFP in multiple slices (Fig 7 C). In most images of Kv2.1-GFP expressing neurons, GxTX-594 labeled punctate were observed on neighboring neurons that did not express Kv2.1-GFP, but at intensities that were roughly an order of magnitude dimmer (Fig 7 B, white arrow). The similarity in the labeling patterns are consistent with GxTX-594 labeling endogenous Kv2 channels.

***GxTX-594 fluorescence responds to neuronal depolarization***

To test whether GxTX-594 labeling of brain slices is consistent with labeling of endogenous Kv2 voltage sensors, we determined whether GxTX-594 labeling responds to voltage changes. First, we looked for Kv2-like labeling patterns on CA1 pyramidal neurons in untransfected brain slices bathed in 100 nM GxTX-594. In two-photon optical sections thinner than the neuronal cell bodies, fluorescent puncta circumscribed dark intracellular spaces (Figure 8 A). This was similar to the patterns of fluorescence in Kv2.1-GFP transfected slices (Figure 7 B), and consistent with the punctate expression pattern of Kv2.1 in CA1 pyramidal neurons seen in fixed brain slices (Misonou 2005). We tested whether the punctate fluorescence was voltage-sensitive by voltage-clamping neurons circumscribed by puncta. To ensure voltage clamp of the neuronal cell body,

slices were bathed in tetrodotoxin to block $Na^+$ channels, and $Cs^+$ was included in the patch pipette solution to block $K^+$ currents. In each experiment, a patch clamp pipette was lowered onto a GxTX-594 labeled neuron, and whole-cell configuration was achieved with the holding potential set to -70 mV. At this point, time-lapse imaging of a two-photon optical section was initiated. Depolarization to 0 mV resulted in loss of fluorescence from a subset of puncta surrounding the voltage-clamped neuron (Fig 8 B, red arrows, Supplemental Movie). Other fluorescent puncta appeared unaltered by the 0 mV step (Fig 8 B, white arrows). To assess if the fluorescence decrease noted in some puncta after a voltage step to 0 mV was due to random fluctuations during imaging, we compared fluorescence of the apparent cell membrane region to regions more distal from the patch-clamped cell body. To quantify this fluorescence change, an ROI 30 pixels (1.2 μm) wide containing the apparent membrane of the cell body was compared to other regions within each image (Fig 8 C). The region containing the membrane of the cell body lost fluorescence during the 0 mV step (Fig 8 D, ROI 1) while neither of the regions more distal (ROI 2, ROI 3), nor the intracellular region (ROI 0) showed a similar change. In multiple slices, the voltage-dependent decrease of fluorescence was pronounced in the region of the neuronal membrane (Fig 8 E). The kinetics of fluorescence response of the voltage-clamped membrane region were similar in multiple slices (Fig 8 F). To determine whether the fluorescence response to depolarization was driven by the Kv2-like puncta on the cell membrane, the fluorescence along a path containing the apparent cell membrane was selected by drawing a path connecting fluorescent puncta surrounding the dark cell body region, and averaging fluorescence in a region 10 pixels wide (0.4 μm) centered on this path (Fig 8 G, yellow line). The fluorescence intensity along the path of the ROI revealed distinct peaks corresponding to puncta (Fig 8 H, red trace). After stepping the neuron to 0 mV, the intensity of fluorescence of a subset of puncta lessened (Fig 8 H, black trace, peaks 1,3,4,5,8). The Scheme II model predicts an 55% reduction of fluorescence, but even more reduction is observed in individual fluorescence puncta in brain slice (Fig 8, I blue line). This would be expected if the concentration of GxTX-594 diminished as it penetrated into the brain tissue (Fig 6 A). However, other puncta which appeared to be on the surface of the same cell body, maintained or increased in brightness (Fig 8 H, black trace, peaks 2, 6, 7). These puncta could possibly represent Kv2 proteins on a neighboring cell, internalized Kv2-GxTX-594 complexes, off-target labeling by GxTX-594, or Kv2 channels that are unresponsive to voltage. When the kinetics of fluorescence intensity decay

of individual voltage-sensitive puncta were fit with Eq. 1, $k_{\Delta F}$ values were similar to each other (Fig 8 I), consistent with these spatially separated puncta all being on the surface of the voltage-clamped neuron.

To address whether the fluorescence change at the cell membrane was driven by decreases in regions of punctate fluorescence, the punctate and non-punctate fluorescence intensity changes were analyzed separately. The regions with fluorescence intensities above average for the path (Fig 8 H, dashed line) were binned as one group, and the regions with below average fluorescence binned as another. The above-average group, by definition, contained all punctate fluorescence. When comparing the fluorescence before and during the 0 mV step, the regions that were initially below average maintained the same intensity (103 ± 8%); regions of above average fluorescence decreased in the intensity (70 ± 8%) (Fig 8 J). This suggests that the detectable unlabeling along the cell membrane originated in the puncta, not the regions of lower fluorescence intensity between them.

To determine whether the voltage-dependent response of GxTX-594 fluorescence from neurons in brain slices could arise from endogenous Kv2.1, we performed experiments with Kv2.1-expressing CHO cells under similar conditions as brain slice: 100 nM GxTX-594, 30°C, $Cs^+$-containing patch pipette solution. Values with 100 nM GxTX-594 on Kv2.1-CHO cells were similar to neurons in brain slices when their voltage was stepped to 0 mV (Fig 8 K). This similarity is consistent with GxTX-594 labeling endogenous channels that have a voltage dependence similar to Kv2.1. Calculations with the model relating GxTX-594 fluorescence to Kv2.1 conformational change predicted the voltage responses seen in neurons. The $k_{\Delta F}$ in response to a 0 mV depolarizing step to neurons in brain slice labeled with 100 nM GxTX-594 was consistent to the $k_{\Delta F}$ of 6.31 x $10^{-2}$ $s^{-1}$ predicted by the statistical thermodynamic for Kv2.1 expressed in CHO cells (Fig 6 B red line, and Fig 8 K blue line). The data are consistent with the voltage sensors of Kv2 channels in hippocampal CA1 neurons having a similar probability of activation at 0 mV as the voltage sensor movement. The fluorescence changes of GxTX-594 in brain slice indicate that the voltage sensors of clustered Kv2 channels in neurons are responsive to voltage and suggests that the voltage response dynamics of Kv2.1 channels expressed in CHO

cells are similar to the dynamics of the endogenous Kv2 channels in CA1 neurons embedded within the hippocampus.

## Discussion

We conclude that GxTX-594 labels endogenous Kv2 channels. This conclusion is based on several metrics. GxTX-594 labels Kv2 proteins (Fig 1), in the presence of its obligate neuronal auxiliary subunit AMIGO-1 (Fig 3), but does not label related, non-Kv2, Kv proteins (Fig 2). Steps to 0 mV resulted in unlabeling of CHO cells (Fig 4) and neurons (Fig 8), and the kinetics of this unlabeling were similar (Fig 8 K). The punctate GxTX-594 labeling of CA1 neurons is consistent with the patterns of endogenous Kv2 expression seen by immunofluorescence (Misonou *et al.* 2005, Bishop *et al.* 2015, 2018), and Kv2.1-GFP expression (Fig 7). Together, these results are consistent with the GxTX-594 probe labeling endogenous Kv2 channels in rat CA1 hippocampal pyramidal neurons and unlabeling in response to voltage activation of the channels. These results indicate that tracking the fluorescence of conformation-dependent ligands such as GxTX-594 can reveal conformational changes of endogenous proteins. Below we discuss physiological questions that could be addressed with a GxTX-based Kv2 voltage sensor probe, the limitations of GxTX-594 as a probe, and the potential for conformation-selective ligands to be engineered into imaging probes for a protein of interest.

### *A voltage sensor probe to study Kv2 physiology*

The GxTX-594 probe is an ECAP that reveals conformational changes of Kv2 voltage sensors. Activation of Kv2 voltage sensors is required for opening of its $K^+$-conductive pore (Islas & Sigworth 1999). Cells dynamically regulate the voltage sensitivity of Kv2 channel pore opening (Murakoshi *et al.* 1997, MacDonald *et al.* 2003, Misonou *et al.* 2005, 2006, Redman *et al.* 2007, Plant *et al.* 2011, Mandikian *et al.* 2014). It is unknown whether these regulatory processes impact voltage sensor movement directly, or impact conformational changes that are coupled to voltage sensor movement, such as pore opening. By specifically measuring voltage sensor movements, the mechanisms by which pore opening is regulated can be better understood. In studies of the mechanism of cellular regulation of Kv2.1 in HEK cells, it was concluded that voltage sensor movements were decoupled from pore opening in the majority of channels with punctate localization (O'Connell *et al.* 2010, Fox *et al.* 2013). This conclusion was supported by assessing movement of voltage sensors with gating currents, currents arising from the movement of voltage sensors themselves. Gating current measurements are feasible only in cell preparations where a sufficiently high density of voltage sensors can be voltage-clamped. This density

requirement has resulted in gating current measurement being most commonly conducted in heterologous expression systems, such as *Xenopus* oocytes or CHO cells. Measurements of endogenous gating currents have been restricted to a limited number of cell preparations such as invertebrate giant axons (Armstrong & Bezanilla 1973) and muscle cells (M. F. Schneider & Chandler 1973). Gating currents or other measures of conformational change of endogenous voltage sensors have never, to our knowledge, been measured in a brain slice.

The GxTX-594 ECAP has revealed the first glimpse of how Kv2 voltage sensors are operating in a tissue. The kinetics of the GxTX-594 response to voltage were similar in brain slice and CHO cells, indicating that the stimulus-response relation between transmembrane voltage and voltage sensor conformational change is similar in the two cell preparations. Our results indicate that the voltage sensors of endogenous Kv2 proteins clustered on the surface of CA1 pyramidal neurons in rat hippocampus are responsive to voltage. This result is perhaps expected, as it is consistent with the proposal of Tamkun and colleagues (Fox *et al.* 2013), who concluded that while only a small fraction of clustered Kv2.1 channels in HEK cells conduct $K^+$ current, many more channels change conformation in response to voltage change. In addition to reporting when and where Kv2 channels enter conformations that are prerequisites for channel opening, Kv2 ECAPs could reveal where nonconducting Kv2 proteins change conformation. Whether conformational changes are important for the growing list of Kv2's nonconducting functions are unknown. By reporting voltage sensor activation, the GxTX-594 probe could potentially be used to determine whether voltage sensor conformational change is crucial for the nonconducting functions of Kv2 proteins.

***Limitations of using GxTX-594 to measure conformational change***

The ability of conformation-selective probes to report conformational change is inherently limited. Some limitations result from the properties of the particular probe deployed, while other limitations are inherent to the mechanism of conformation-selective binding. Below, we discuss limitations of GxTX-594 and how those limitations can be managed in the realms of temporal resolution, signal to noise, protein modulation by probes, and errors in interpretation of images.

*Temporal resolution.* With GxTX-594, the average probability that voltage sensors are activated ($P_{active}$), can be measured. GxTX-594 requires seconds to respond, much slower than the membrane voltage changes associated with action potentials. Probes with faster kinetics are expected to enable measurements of faster patterns of channel activity. Modifying probe kinetics becomes a question of sensor design and toxin engineering; the response properties of probes can be altered by chemical modification of side chain residues, allowing the dynamics to be optimized in next-generation probes. Ultimately the response time of any conformation-selective probe will be limited by the labeling rate which is a product of the probe's concentration and its inherent association constant. Alternatively, ECAPs that remain bound while producing a fluorescence change in response to their target's conformational change could provide much faster time resolution.

*Signal to noise.* The fluorescence signal intensity from GxTX-594 limited spatial and temporal resolution, estimates of $P_{active}$, and interpretation of data. Continuing advances in microscopy are expected to improve fundamental signal to noise of fluorescence imaging in tissue. However, the signal to noise in all experiments is ultimately limited by the photophysics of the fluorophore as well as photodamage to the probe and tissue. Probes with improved fluorescence characteristics are expected to improve the ultimate signal to noise. Quantum dot nanoparticles offer orders of magnitude improvement in signal to noise for one- and two-photon excitation microscopy methods. We have developed synthetic methods for making Kv2 quantum dot ECAPs from GxTX (Mann *et al.* 2018). These probes are expected to respond to Kv2 channel voltage sensor activation with similarly interpretable fluorescence changes, yet offer orders of magnitude improvements in signal to noise ratio.

*Protein modulation by probes.* GxTX-based probes inhibit the Kv2 channels they label. Thus, they deplete the population of channels responding normally to physiological stimuli. This is a general problem with molecular probes: they disrupt the process they report (e.g. free calcium indicators deplete free calcium). This probe perturbation problem can be minimized by working with low concentrations of probe to inhibit a minimal subset of the total Kv2 population. Channel activity can be recorded optically even when only a small fraction of Kv2 channels are affected (Tilley *et al.* 2014). Furthermore, GxTX-594 most accurately reports conformational

change when used at sub-saturating concentrations (Fig 6). Thus, low concentrations are optimal for both accuracy of measurement and minimizing the perturbation of physiology.

*Errors in interpretation of images.* The models enabling quantification of conformational change involve approximations. The statistical thermodynamics developed here involve ligand binding and conformational change dynamics using approximations of Eyring rate theory (Eyring 1935a, b). Thus, models will always have limitations stemming from the necessary approximations. The model of Kv2 voltage sensor conformational change developed here is an oversimplification. While the gating dynamics of Kv2 channels have never been fully described with an explicit thermodynamic model, they are certainly more complex than our model. Our model assumes each of the of the channel's 4 voltage sensors bind 1 GxTX, and that the 4 voltage sensors change conformation independently of each other. However, Kv2 channels exhibit cooperative gating when they open their pores, and pore opening impacts voltage sensors (Islas & Sigworth 1999, Scholle, Dugarmaa, *et al.* 2004, Jara-Oseguera *et al.* 2011, Tilley *et al.* 2019). Under some conditions the assumption of voltage sensor independence may limit the model's predictive power. Additionally, the model of GxTX-594 labeling developed here assumes that voltage sensors are in continuous equilibrium. This simplification is expected to result in diminished accuracy during high frequency voltage changes, such as during action potentials. These deviations from equilibrium could explain the deviation of the model from the data in response to high frequency voltage steps (Fig 5 C, D).

***Conformation-selective probes reveal conformational change of endogenous proteins***

If the limitations of conformation-selective binding are given adequate consideration, deconvolution of fluorescence intensities can reveal conformational changes of endogenous proteins. Importantly, measurements of dynamic labeling by a conformation-selective probe, such as GxTX, can enable deduction of how unlabeled proteins behave, despite the fact that GxTX nearly completely inhibits Kv2 voltage sensor movement of the subunit it binds, and only proteins that are labeled with a fluorescent GxTX-based probe generate optical signals (Tilley *et al.* 2014, 2019). This approach is analogous to calcium imaging experiments, which have been spectacularly informative about physiological calcium signaling (W. Yang & Yuste 2017), despite the fact that no optical signals originate from the physiologically relevant free $Ca^{2+}$, only

from $Ca^{2+}$ that is chelated by a dye. In all such experiments, fluorescence from $Ca^{2+}$-bound dyes is deconvolved using the statistical thermodynamics of $Ca^{2+}$ binding to calculate free $Ca^{2+}$(Adams 2010). Similarly, GxTX-based probes are dynamically binding to unlabeled Kv2 proteins, and the binding rate is dependent on the probability that unlabeled voltage sensors are in a resting conformation (Fig 6). Thus, the conformations of unlabeled Kv2 proteins influence the dynamics of labeling with GxTX-based probes. Consequently, the dynamics of labeling reveal the conformations of unlabeled Kv2 proteins.

Deployment of GxTX-594 to report conformational changes of endogenous channels demonstrates that conformation-selective ligands can be used to image occurrence of the conformations they bind to. The same principles of action apply to any conformation-selective labeling reagent, suggesting that probes for conformational changes of many different proteins could be developed. Probes could conceivably be developed from the many other voltage sensor toxins and other gating modifiers that act by a similar mechanism as GxTX, yet target the voltage sensors of different ion channel proteins (McDonough *et al.* 1997, Sack *et al.* 2004, Catterall *et al.* 2007, Swartz 2007, Schmalhofer *et al.* 2008, Peretz *et al.* 2010, McCormack *et al.* 2013, Ahuja *et al.* 2015, A. H. Zhang *et al.* 2018, Dockendorff *et al.* 2018). Conformation-selective binders have been engineered for a variety of other proteins, yet methods to quantify conformational changes from their fluorescence are needed. For example, fluorescently-labeled conformation-selective binders have enable novel studies GPCR signaling (Irannejad *et al.* 2013). These GPCR probes are GFP-tagged recombinant camelid antibodies that bind to GPCRs with enhanced affinity when the GPCRs adopt activated conformations. GPCR probes have revealed that endocytosed GPCRs continue to remain in a physiologically active conformation, leading to the proposition that substantial GPCR signaling takes place in endosomes (Tsvetanova *et al.* 2015, Eichel & von Zastrow 2018). However, a means to determine the conformational equilibria of GPCRs from probe fluorescence has not yet been developed. The statistical thermodynamic framework developed here could provide a starting point for more quantitative interpretation of time-lapse imaging of other conformation-selective probes.

Probes such as GxTX-594 that bind select conformations of ion channels are expected to have the general response properties displayed in Figure 6. That is, as the equilibrium between conformations changes, the probe will label or unlabel at different rates. Importantly, when concentrations of a probe are less than the apparent $K_d$, fluorescence change becomes proportional to conformational change of unlabeled proteins. We suggest that generation of further conformation-dependent probes and models to interpret their fluorescence could allow the measurement of conformational equilibria of a wide variety of endogenous proteins.

## Materials and methods

### *GxTX-594 synthesis*

The GxTX peptide used was a guangxitoxin-1E variant with methionine 35 was replaced by the oxidation-resistant noncanonical amino acid norleucine (Tilley *et al.* 2014). GxTX was functionalized by replacement of serine 13 with cysteine to create a spinster thiol. The GxTX-Cys13 peptide was synthesized as described (Tilley *et al.* 2014). GxTX was labeled with a Texas red derivative (Alexa Fluor 594 $C_5$ maleimide, Thermo Fisher Scientific, Catalog # 10256). To label the peptide, GxTX lyophilisate was brought to 560 μM in 50% ACN + 1 mM $Na_2EDTA$. 2.4 μL of 1M Tris (pH 6.8 with HCl), 4 μL of 10 mM of Alexa Fluor 594 $C_5$ maleimide in DMSO and 17.9 μL of 560 μM GxTX-Cys13 were added for a final solution of 100 mM Tris, 1.6 mM Alexa Fluor 594 $C_5$ maleimide and 0.412 mM GxTX in 24.33 μL of reaction solution. Reactants were mixed in a 1.5 mL low protein binding polypropylene tube (LoBind, Eppendorf, Catalog # 022431081) and mixed at 1000 RPM, 20°C for 4 hours (Thermomixer 5355 R, Eppendorf). After incubation, the tube was centrifuged at 845 RCF for 10 minutes at room temperature. A purple pellet was observed post-centrifugation. The supernatant was transferred to a fresh tube and centrifuged at 845 RCF for 10 minutes. After this 2$^{nd}$ centrifugation, no visible pellet was seen. The supernatant was injected onto a reverse-phase HPLC $C_{18}$ column (Biobasic- 4.6mm RP-$C_{18}$ 5 μm, Thermo Fisher Scientific, Catalog # 2105-154630) equilibrated in 20% ACN, 0.1% TFA at 1 mL/min and eluted with a protocol holding in 20% ACN for 2 minutes, increasing to 30% ACN over 1 minute, then increasing ACN at 0.31% per minute. HPLC effluent was monitored by fluorescence and an absorbance array detector. 1 ml fractions were pooled based on fluorescence (280 nm excitation, 350 nm emission) and absorbance (214 nm, 280 nm and 594 nm). GxTX-594 peptide-fluorophore conjugate eluted at approximately 35% ACN, and mass was confirmed by mass spectrometry using a Bruker UltraFlextreme MALDI-TOF/TOF (Fig 1 Supplement 1). Samples for identification from HPLC eluant were mixed 1:1 in an aqueous solution of 25% MeOH and 0.05% TFA saturated with alpha-cyano-4-hydrocinnamic acid. Briefly, mixed samples were pipetted onto a ground-steel plate, dried under vacuum, and ionized with 60-80% laser power. Molecular species were detected using a reflector mode protocol and quantitated using Bruker Daltonics flexAnalysis 3.4. Conjugation product was dissolved in CE buffer (defined below), and stored at -80 °C. GxTX-594 concentration was

determined by 280 nm absorbance using a calculated extinction coefficient of 18,900 A.U. $M^{-1}$ $cm^{-1}$.

***CHO cell methods***

*CHO cell culture and transfection*

The CHO-K1 cell line (ATCC) and a variant stably transfected with a tetracycline-inducible rat Kv2.1 construct (Kv2.1-CHO) (Trapani & Korn 2003), were cultured as described previously (Tilley *et al.* 2014). To induce channel expression in Kv2.1-TREx-CHO cells, 1 µg/mL minocycline (Enzo Life Sciences, Catalog # ALX-380-109-M050), prepared in 70% ethanol at 2 mg/mL, was added to the maintenance media to induce $K^+$ expression. Minocycline was added 40-48 hours before imaging and voltage clamp fluorometry experiments. Transfections were achieved with Lipofectamine 2000 (Life Technologies, Catalog # 1668027). 1.1 µL of Lipofectamine was diluted, mixed, and incubated in 110 µL of Opti-MEM (Gibco, Product Number 31985-062, Lot Number 1917064) in a 1:100 ratio for 5 minutes at room temperature. Concurrently, 1 µg of plasmid DNA and 110 µL of Opti-MEM were mixed in the same fashion. DNA and Lipofectamine 2000 mixtures were combined, titurated, and let sit for 20 minutes. Then, transfection cocktail mixture was added to freshly seeded cells at approximately 40% confluency and allowed to settle at 37°C. The transfection cocktail was added to cells for 4-6 hours before the media was replaced. Rat Kv2.1-GFP (Antonucci *et al.* 2001), rat Kv2.2-GFP (Kirmiz, Vierra, *et al.* 2018), rat Kv1.5-GFP (H. Li *et al.* 2001), rat Kv4.2-GFP (Shibata *et al.* 2003), mouse BK-GFP (Trimmer Lab, UC Davis), rat Kv2.1 S586A-GFP (Kirmiz, Palacio, *et al.* 2018), rat AMIGO-YFP (Bishop *et al.* 2015), rat KvBeta2 (Shibata *et al.* 2003) and rat KCHiP2 (An *et al.* 2000) plasmids were all kind gifts from James Trimmer, University of California, Davis. Identities of constructs were confirmed by sequencing from their CMV promoter.

*Confocal and Airy disk imaging*

Confocal images were obtained with an inverted confocal system (Zeiss LSM 880 410900-247-075) run by ZEN black v2.1. A 63x/1.40 NA Oil DIC objective (Zeiss 420782-9900-799) was used for most imaging experiments; a 63x/1.2 NA Water DIC objective (Zeiss 441777-9970-000) was used for voltage clamp fluorometry experiments. GFP and YFP were excited with the 488 nm line from an argon laser (3.2 mW at installation) powered at 0.5% unless otherwise

noted. GxTX594 was excited with 594 nm helium-neon laser (0.6 mW at installation) powered at 10% unless otherwise noted. WGA-405 was excited with a 405 nm diode laser, (3.5 mW at installation) powered at 1% unless otherwise noted. Temperature inside the microscope housing was 27-30 °C.

In confocal imaging mode, fluorescence was collected with the microscope's 32-channel gallium arsenide phosphide detector array arranged with a diffraction grating to measure 400-700 nm emissions in 9.6 nm bins. Emission bands were 495-550 nm for GFP and YFP, 605-700 nm for GxTX-594, and 420-480 nm for WGA-405. Point spread functions were calculated using ZEN black software using emissions from 0.1 μm fluorescent microspheres, prepared on a slide according to manufacturer's instructions (Thermo Fisher Scientific, Catalog # T7279). The point spread functions for confocal images with the 63x/1.40 Oil DIC objective in the X-Y direction were 228 nm (488 nm excitation) and 316 nm (594 nm excitation).

In Airy disk imaging mode, fluorescence was collected with the microscope's 32-channel gallium arsenide phosphide detector array arranged in a concentric hexagonal pattern (Zeiss Airyscan 410900-2058-580). After deconvolution, the point spread functions for the 63x/1.40 NA objective with 488 nm excitation was 124 nm in X-Y and 216 nm in Z; with 594 nm excitation 168 nm in X-Y and 212 nm in Z. For the 63x/1.2 NA objective, the point spread function with 488 nm excitation was 187 nm in X-Y and 214nm in Z; the point spread function with 594 nm excitation was 210 nm in X-Y and 213 nm in Z.

Unless stated otherwise, cells were plated in uncoated 35 mm dishes with a 7 mm inset No. 1.5 coverslip (MatTek, Catalog # P35G-1.5-20-C). The CHO cell external (CE) solution used for imaging and electrophysiology contained (in mM): 3.5 KCl, 155 NaCl, 10 HEPES, 1.5 $CaCl_2$, 1 $MgCl_2$, adjusted to pH 7.4 with NaOH. Measured osmolarity was 315 mOsm. When noted, solution was supplemented with either 10 mM glucose (CEG) or 10 mM glucose and 1% BSA (CEGB).

For time-lapse, GxTX-594 dose-response experiments, Kv2.1-CHO cells were plated onto 22 x 22 mm No. 1.5H High Precision coverslips (Deckglaser). Prior to imaging, cell maintenance

media was removed and replaced with CEGB, then incubated in the microscope chamber with indicated concentrations of GxTX-594 for 10 minutes followed by manual wash-out with CEGB solution. 15 minutes after wash-out, the next GxTX-594 concentration was added. Washout and toxin solutions were added manually via a syringe into a ~100 µL perfusion chamber (Warner Instrument, Catalog # RC-24N). Flow rate was ~1 mL / 10 sec. Images were taken every 5 sec. Laser power was set to 0.5% for the 488 nm laser and 1.5% for the 594 nm laser. For colocalization experiments with GFP-tagged proteins, cells were incubated in 100 nM GxTX594 for 5 minutes and then washed with CEGB before imaging.

*Whole cell voltage clamp for CHO cell imaging*

Kv2.1-TREx-CHO cells plated in glass-bottom 35 mm dishes were washed with CEGB, placed in the microscope, and then incubated in 100 µL of 100 nM GxTX594 for 5 minutes to label cells. Before patch clamp, the solution was diluted with 1 mL of CEG for a working concentration of 9 nM GxTX594 during experiments. Cells with obvious GxTX-594 surface staining were voltage-clamped in whole-cell mode with an EPC-10 patch clamp amplifier (HEKA) run by Patchmaster software, v2x90.2 (HEKA). The patch pipette contained a potassium-deficient $Cs^+$ internal pipette solution to limit outward current and reduce voltage error: 70 mM CsCl, 50 mM CsF, 35mM NaCl, 1 mM EGTA, 10 mM HEPES, brought to pH 7.4 with CsOH. Osmolarity was 310 mOsm. The liquid junction potential was calculated to be 3.5 mV and was not corrected. Borosilicate glass pipettes (Sutter Instruments, Catalog # BF 150-110-10HP) were pulled with blunt tips to resistances less than 3.0 MΩ in these solutions. Cells were held at -80 mV (unless noted otherwise) and stepped to indicated voltages. The voltage step stimulus was maintained until any observed change in fluorescence was complete. For stimulus-frequency dependence experiments, cells were given 2 ms steps to 40 mV at stated frequencies (0.02, 5, 10, 20, 50, 100, 150, or 200 Hz). Images for voltage clamp fluorometry were taken in Airy disk imaging mode with the settings described above.

*Whole cell voltage clamp for CHO cell $K^+$ current recordings*

Whole-cell voltage clamp was used to measure currents from CHO cells expressing Kv2.1-GFP, Kv2.2-GFP, Kv1.5-GFP, Kv4.2-GFP, BK-GFP or GFP that we transfected as described above. Cells were plated on glass bottom dishes. Cells were held at -80 mV, then 100 ms voltage steps

were delivered ranging from -80 mV to +80 mV in +5 mV increments. Pulses were repeated every 2 seconds. The external (bath) solution contained CE solution. The internal (pipette) solution contained (in mM): 35 KOH, 70 KCl, 50 KF, 50 HEPES, 5 EGTA adjusted to pH 7.2 with KOH. Liquid junction potential was calculated to be 7.8 mV and was not corrected. Borosilicate glass pipettes (Sutter Instruments, Cat # BF150-110-10HP) were pulled into pipettes with resistance less than 3 MΩ for patch clamp recording. Recordings were at room temperature (22–24 °C). Voltage clamp was achieved with an Axon Axopatch 200B amplifier (MDS Analytical Technologies) run by Pachmaster software, v2x90.2 (HEKA). Holding potential was -80 mV. Capacitance and Ohmic leak were subtracted using a P/5 protocol. Recordings were low pass filtered at 10 kHz and digitized at 100 kHz. Voltage clamp data were analyzed and plotted with Igor Pro 7 or 8 (Wavemetrics). Current amplitudes at each voltage were the average from 0.19-0.20 s after voltage step. As the experiments plotted in Figure 6 Supplement 1 A were merely to confirm functional expression of ion channels at the cell surface, series resistance compensation was not used and substantial cell voltage errors are predicted during these experiments.

***Brain slice methods***

*Hippocampal slice culture preparation and transfection*

All experimental procedures were approved by the University of California Davis Institutional Animal Care and Use Committee and were performed in strict accordance with the Guide for the Care and Use of Laboratory Animals of the NIH. Animals were maintained under standard light dark cycles and had ad libitum access to food and water. Organotypic hippocampal slice cultures were prepared from postnatal day 5-7 rats, as described (Stoppini *et al.* 1991) and detailed in a video protocol (Opitz-Araya & Barria 2011). DIV15-30 neurons were transfected 2-6 days before imaging via biolistic gene transfer (160 psi, Helios gene gun, Bio-Rad), as described in the detailed video protocol (Woods & Zito 2008). 10 µg of plasmid was coated to 6-8 mg of 1.6 µm gold beads.

*Two-photon slice imaging*

Image stacks (512 x 512 pixels, 1 mm Z-steps; 0.035 µm/pixel) were acquired using a custom 2-photon microscope (Olympus LUMPLFLN 60XW/IR2 objective, 60x, 1.0 NA) with two pulsed

Ti:sapphire lasers (Mai Tai: Spectra Physics) tuned to 810 nm (for GxTX594 imaging) and 930 nm (for GFP imaging) and controlled with ScanImage (Pologruto *et al.* 2003). After identifying a neuron expressing Kv2.1-GFP, perfusion was stopped and GxTX-594 was added to the static bath solution to a final concentration of 100 nM. After five minutes incubation, perfusion was restarted, leading to wash-out of GxTX-594 from the slice bath. Red and green photons (Chroma: 565dcxr, BG-22 glass, HQ607/45) emitted from the sample were collected with two sets of photomultiplier tubes (Hamamatsu R3896).

*Whole cell voltage clamp for brain slice imaging*

Organotypic hippocampal slice cultures (DIV 6-7, not transfected) were transferred to an imaging chamber with recirculating ACSF maintained at 30°C. To hold the slice to the bottom of the chamber, a horseshoe-shaped piece of gold wire was used to weight the membrane holding the slice. ACSF contained (in mM) 127 NaCl, 25 $NaHCO_3$, 25 D-glucose, 2.5 KCl, 1.25 $NaH_2PO_4$, 1 MgCl2, 2 $CaCl_2$, 200 nM tetrodotoxin, pH 7.3 and aerated with 95% $O_2$/ 5% $CO_2$ (~310mOsm). 4 mL of 100 nM GxTX-594 in ACSF were used in the circulating bath to allow the toxin to reach the slice and reach the desired concentration of 100 nM throughout the circulating bath. Images were acquired beginning 3 minutes after GxTX-594 was added. Apparent CA1 neurons with GxTX-594 labeling in a Kv2-like pattern were selected for whole-cell patch clamp. Voltage clamp was achieved using an Axopatch 200B amplifier (Axon Instruments) controlled with custom software written in Matlab (MathWorks, Inc.). Patch pipettes (5-7 MΩ) were filled with intracellular solution containing (in mM): 135 Cs-methanesulfonate, 10 $Na_2$-phosphocreatine, 3 Na-L-ascorbate, 4 NaCl, 10 HEPES, 4 $MgCl_2$, 4 $Na_2ATP$, 0.4 NaGTP, pH 7.2. Neurons were clamped at -70 mV. Input resistance and holding current were monitored throughout the experiment. Cells were excluded if the pipette series resistance was higher than 25 MΩ or if the holding current exceeded -100 pA. To activate Kv2 channels, a 50 s depolarizing step from -70 mV to 0 mV was given.

***Image analysis***

Fluorescence images were analyzed using ImageJ 1.52n software (C. A. Schneider *et al.* 2012). Regions of interest (ROIs) were drawn manually, as described. Unless mentioned otherwise, the ROI encompassed the entire fluorescent region of an individual cell or neuron. Fluorescence

intensity ($F$) was background subtracted using mean F of a region lacking cells. For $F/F_{init}$ normalization, $F$ was the mean preceding stimuli, or the max observed intensity in dose response experiments. Time dependence of fluorescence intensity was fit with a monoexponential decay (Eq. 1). $F_o$ corresponds to initial intensity and $t_o$ corresponds to initial time. The variables $A$, $t$ and $\tau$ correspond to the amplitude, time and rate constant, respectively. For colocalization analyses the Pearson coefficient was calculated using the JACoP plugin (Bolte & Cordelières 2006). Colocalization analyses were conducted within ROIs defining individual cells. Plotting and curve fitting was performed with IgorPro software (Wavemetrics), which performs nonlinear least-squares fits using a Levenberg-Marquardt algorithm. Error values from individual curve fittings are standard deviations. All other errors, including error bars, indicate standard errors. Arithmetic means are reported for intensity measurements and correlation coeffcients. Geometric means are reported for time constants and rates. Statistical comparisons were with the Mann-Whitney U test.

**Acknowledgements**

We thank Jim Trimmer (University of California, Davis) for numerous discussions, and constructive critical reading of an early version of the manuscript. We thank Georgeann Sack (Afferent, LLC) for critical reading, editing, and feedback.

This research was supported by US National Institutes of Health grants R01NS096317, U01NS090581, R21EY026449, and T32GM007377. P. Thapa was supported by American Heart Association postdoctoral fellowship 17POST33670698. GxTX variants were synthesized at the Molecular Foundry of the Lawrence Berkeley National Laboratory under US Department of Energy contract DE-AC02-05CH11231.

The authors declare no competing financial interests.

**Author contributions (CRediT nomenclature)**

Parashar Thapa: Conceptualization, Formal analysis, Investigation, Methodology, Visualization, Writing- original draft, Writing- reviewing & editing

Robert Stewart: Conceptualization, Formal analysis, Investigation, Methodology, Visualization, Writing- original draft, Writing- reviewing & editing

Rebecka J. Sepela: Conceptualization, Formal analysis, Investigation, Methodology, Visualization, Writing- original draft, Writing- reviewing & editing

Oscar Vivas: Investigation, Methodology, Writing- reviewing & editing

Laxmi K. Parajuli: Investigation, Methodology, Writing- reviewing & editing

Mark Lillya: Conceptualization, Formal analysis, Investigation, Methodology, Visualization

Sebastian Fletcher-Taylor: Investigation, Methodology, Writing- reviewing & editing

Bruce E. Cohen: Conceptualization, Funding acquisition, Project administration, Supervision, Writing- reviewing & editing

Karen Zito: Conceptualization, Funding acquisition, Investigation, Methodology, Project administration, Supervision, Writing- original draft, Writing- reviewing & editing

Jon T. Sack: Conceptualization, Formal analysis, Funding acquisition, Investigation, Methodology, Project administration, Supervision, Visualization, Writing- original draft, Writing- reviewing & editing

## References


Adams, S.R. (2010) How calcium indicators work. *Cold Spring Harbor Protocols*, **2010**, pdb.top70. doi:10.1101/pdb.top70

Aggarwal, S.K. & MacKinnon, R. (1996) Contribution of the S4 segment to gating charge in the Shaker K+ channel. *Neuron*, **16**, 1169–77. doi:10.1016/S0896-6273(00)80143-9

Ahuja, S., Mukund, S., Deng, L., Khakh, K., Chang, E., Ho, H., Shriver, S., *et al.* (2015) Structural basis of Nav1.7 inhibition by an isoform-selective small-molecule antagonist. *Science*, **350**, aac5464. doi:10.1126/science.aac5464

Amberg, G.C., Rossow, C.F., Navedo, M.F. & Santana, L.F. (2004) NFATc3 regulates Kv2.1 expression in arterial smooth muscle. *The Journal of Biological Chemistry*, **279**, 47326–34. doi:10.1074/jbc.M408789200

An, W.F., Bowlby, M.R., Betty, M., Cao, J., Ling, H.P., Mendoza, G., Hinson, J.W., *et al.* (2000) Modulation of A-type potassium channels by a family of calcium sensors. *Nature*, **403**, 553–556. doi:10.1038/35000592

Antonucci, D.E., Lim, S.T., Vassanelli, S. & Trimmer, J.S. (2001) Dynamic localization and clustering of dendritic Kv2.1 voltage-dependent potassium channels in developing hippocampal neurons. *Neuroscience*, **108**, 69–81. doi:10.1016/S0306-4522(01)00476-6

Armstrong, C.M. & Bezanilla, F. (1973) Currents related to movement of the gating particles of the sodium channels. *Nature*, **242**, 459–61. doi:10.1038/242459a0

Baver, S.B., Hope, K., Guyot, S., Bjørbaek, C., Kaczorowski, C. & O'Connell, K.M.S. (2014) Leptin modulates the intrinsic excitability of AgRP/NPY neurons in the arcuate nucleus of the hypothalamus. *The Journal of Neuroscience*, **34**, 5486–96. doi:10.1523/JNEUROSCI.4861-12.2014

Bestvater, F., Spiess, E., Stobrawa, G., Hacker, M., Feurer, T., Porwol, T., Berchner-Pfannschmidt, U., *et al.* (2002) Two-photon fluorescence absorption and emission spectra of dyes relevant for cell imaging. *Journal of Microscopy*, **208**, 108–15. doi:10.1046/j.1365-2818.2002.01074.x.

Bezanilla, F. (2018) Gating currents. *The Journal of General Physiology*, **150**, 911–932. doi:10.1085/jgp.201812090

Bishop, H.I., Cobb, M.M., Kirmiz, M., Parajuli, L.K., Mandikian, D., Philp, A.M., Melnik, M., *et al.* (2018) Kv2 Ion Channels Determine the Expression and Localization of the Associated AMIGO-1 Cell Adhesion Molecule in Adult Brain Neurons. *Frontiers in Molecular Neuroscience*, **11**, 1. doi:10.3389/fnmol.2018.00001

Bishop, H.I., Guan, D., Bocksteins, E., Parajuli, L.K., Murray, K.D., Cobb, M.M., Misonou, H., *et al.* (2015) Distinct Cell- and Layer-Specific Expression Patterns and Independent Regulation of Kv2 Channel Subtypes in Cortical Pyramidal Neurons. *The Journal of Neuroscience*, **35**, 14922–42. doi:10.1523/JNEUROSCI.1897-15.2015

Blaine, J.T. & Ribera, A.B. (2001) Kv2 channels form delayed-rectifier potassium channels in situ. *The Journal of Neuroscience*, **21**, 1473–80. doi:10.1523/jneurosci.21-05-01473.2001

Bocksteins, E. (2016) Kv5, Kv6, Kv8, and Kv9 subunits: No simple silent bystanders. *The Journal of General Physiology*, **147**, 105–25. doi:10.1085/jgp.201511507

Bolte, S. & Cordelières, F.P. (2006) A guided tour into subcellular colocalization analysis in light microscopy. *Journal of Microscopy*, **224**, 213–32. doi:10.1111/j.1365-2818.2006.01706.x

Catterall, W.A., Cestèle, S., Yarov-Yarovoy, V., Yu, F.H., Konoki, K. & Scheuer, T. (2007) Voltage-gated ion channels and gating modifier toxins. *Toxicon*, **49**, 124–141. doi:10.1016/j.toxicon.2006.09.022

Cobb, M.M., Austin, D.C., Sack, J.T. & Trimmer, J.S. (2016) Cell cycle-dependent changes in localization and phosphorylation of the plasma membrane Kv2.1 $K^+$ channel impact endoplasmic reticulum membrane contact sites in COS-1 cells. *Journal of Biological Chemistry*, **291**, 5527–5527. doi:10.1074/jbc.A115.690198

Cotella, D., Hernandez-Enriquez, B., Wu, X., Li, R., Pan, Z., Leveille, J., Link, C.D., *et al.* (2012) Toxic Role of K+ Channel Oxidation in Mammalian Brain. *Journal of Neuroscience*, **32**, 4133–4144. doi:10.1523/JNEUROSCI.6153-11.2012

Dai, X.-Q., Kolic, J., Marchi, P., Sipione, S. & MacDonald, P.E. (2009) SUMOylation regulates Kv2.1 and modulates pancreatic  -cell excitability. *Journal of Cell Science*, **122**, 775–779. doi:10.1242/jcs.036632

de Kovel, C.G.F., Syrbe, S., Brilstra, E.H., Verbeek, N., Kerr, B., Dubbs, H., Bayat, A., *et al.* (2017) Neurodevelopmental Disorders Caused by De Novo Variants in KCNB1 Genotypes and Phenotypes. *JAMA Neurology*, **74**, 1228–1236. doi:10.1001/jamaneurol.2017.1714

Dockendorff, C., Gandhi, D.M., Kimball, I.H., Eum, K.S., Rusinova, R., Ingólfsson, H.I., Kapoor, R., *et al.* (2018) Synthetic Analogues of the Snail Toxin 6-Bromo-2-mercaptotryptamine Dimer (BrMT) Reveal That Lipid Bilayer Perturbation Does Not Underlie Its Modulation of Voltage-Gated Potassium Channels. *Biochemistry*, **57**, 2733–2743. doi:10.1021/acs.biochem.8b00292

Du, J., Haak, L.L., Phillips-Tansey, E., Russell, J.T. & McBain, C.J. (2000) Frequency-dependent regulation of rat hippocampal somato-dendritic excitability by the K+ channel subunit Kv2.1. *The Journal of Physiology*, **522 Pt 1**, 19–31. doi:10.1111/j.1469-7793.2000.t01-2-00019.xm

Du, J., Tao-Cheng, J.-H., Zerfas, P. & McBain, C.. (1998) The K+ channel, Kv2.1, is apposed to astrocytic processes and is associated with inhibitory postsynaptic membranes in hippocampal and cortical principal neurons and inhibitory interneurons. *Neuroscience*, **84**, 37–48. doi:10.1016/S0306-4522(97)00519-8

Eichel, K. & Zastrow, M. von. (2018) Subcellular Organization of GPCR Signaling. *Trends in Pharmacological Sciences*, **39**, 200–208. doi:10.1016/j.tips.2017.11.009

Eyring, H. (1935) The Activated Complex and the Absolute Rate of Chemical Reactions. *Chemical Reviews*, **17**, 65–77, American Chemical Society. doi:10.1021/cr60056a006

Eyring, H. (1935) The Activated Complex in Chemical Reactions. *The Journal of Chemical Physics*, **3**, 107–115, American Institute of Physics. doi:10.1063/1.1749604

Feinshreiber, L., Singer-Lahat, D., Friedrich, R., Matti, U., Sheinin, A., Yizhar, O., Nachman, R., *et al.* (2010) Non-conducting function of the Kv2.1 channel enables it to recruit vesicles for release in neuroendocrine and nerve cells. *Journal of Cell Science*, **123**, 1940–7. doi:10.1242/jcs.063719

Fox, P.D., Haberkorn, C.J., Akin, E.J., Seel, P.J., Krapf, D. & Tamkun, M.M. (2015) Induction of stable ER-plasma-membrane junctions by Kv2.1 potassium channels. *Journal of Cell Science*, **128**, 2096–105. doi:10.1242/jcs.166009

Fox, P.D., Loftus, R.J. & Tamkun, M.M. (2013) Regulation of Kv2.1 K(+) conductance by cell surface channel density. *The Journal of Neuroscience*, **33**, 1259–70. doi:10.1523/JNEUROSCI.3008-12.2013

Fu, J., Dai, X., Plummer, G., Suzuki, K., Bautista, A., Githaka, J.M., Senior, L., *et al.* (2017) Kv2.1 Clustering Contributes to Insulin Exocytosis and Rescues Human β-Cell Dysfunction. *Diabetes*, **66**, 1890–1900. doi:10.2337/db16-1170

Gamper, N., Stockand, J.D. & Shapiro, M.S. (2005) The use of Chinese hamster ovary (CHO) cells in the study of ion channels. *Journal of Pharmacological and Toxicological Methods*, **51**, 177–85. doi:10.1016/j.vascn.2004.08.008

Gilchrist, J., Das, S., Petegem, F. Van & Bosmans, F. (2013) Crystallographic insights into sodium-channel modulation by the β4 subunit. *Proceedings of the National Academy of Sciences of the United States of America*, **110**, E5016-24. doi:10.1073/pnas.1314557110

Gupta, K., Zamanian, M., Bae, C., Milescu, M., Krepkiy, D., Tilley, D.C., Sack, J.T., *et al.* (2015) Tarantula toxins use common surfaces for interacting with Kv and ASIC ion channels. *eLife*, **4**, e06774. doi:10.7554/eLife.06774

Herrington, J., Zhou, Y.P., Bugianesi, R.M., Dulski, P.M., Feng, Y., Warren, V.A., Smith, M.M., *et al.* (2006) Blockers of the Delayed-Rectifier Potassium Current in Pancreatic β-cells Enhance Glucose-Dependent Insulin Secretion. *Diabetes*, **55**, 1034–1042. doi:10.2337/diabetes.55.04.06.db05-0788

Hönigsperger, C., Nigro, M.J. & Storm, J.F. (2017) Physiological roles of Kv2 channels in entorhinal cortex layer II stellate cells revealed by Guangxitoxin-1E. *The Journal of Physiology*, **595**, 739–757. doi:10.1113/JP273024

Irannejad, R., Tomshine, J.C., Tomshine, J.R., Chevalier, M., Mahoney, J.P., Steyaert, J., Rasmussen, S.G.F., *et al.* (2013) Conformational biosensors reveal GPCR signalling from endosomes. *Nature*, **495**, 534–8. doi:10.1038/nature12000

Islas, L.D. & Sigworth, F.J. (1999) Voltage sensitivity and gating charge in Shaker and Shab family potassium channels. *The Journal of General Physiology*, **114**, 723–42. doi:10.1085/jgp.114.5.723

Jacobson, D.A., Kuznetsov, A., Lopez, J.P., Kash, S., Ammälä, C.E. & Philipson, L.H. (2007) Kv2.1 ablation alters glucose-induced islet electrical activity, enhancing insulin secretion. *Cell Metabolism*, **6**, 229–35. doi:10.1016/j.cmet.2007.07.010

Jara-Oseguera, A., Ishida, I.G., Rangel-Yescas, G.E., Espinosa-Jalapa, N., Pérez-Guzmán, J.A., Elías-Viñas, D., Lagadec, R. Le, *et al.* (2011) Uncoupling charge movement from channel opening in voltage-gated potassium channels by ruthenium complexes. *The Journal of Biological Chemistry*, **286**, 16414–25. doi:10.1074/jbc.M110.198010

Jegla, T., Marlow, H.Q., Chen, B., Simmons, D.K., Jacobo, S.M. & Martindale, M.Q. (2012) Expanded functional diversity of shaker K(+) channels in cnidarians is driven by gene expansion. (Z. Zhang, Ed.)*PlOS ONE*, **7**, e51366. doi:10.1371/journal.pone.0051366

Johnson, B., Leek, A.N., Solé, L., Maverick, E.E., Levine, T.P. & Tamkun, M.M. (2018) Kv2 potassium channels form endoplasmic reticulum/plasma membrane junctions via interaction with VAPA and VAPB. *Proceedings of the National Academy of Sciences of the United States of America*, **115**, E7331–E7340. doi:10.1073/pnas.1805757115

Kihira, Y., Hermanstyne, T.O. & Misonou, H. (2010) Formation of Heteromeric Kv2 Channels in Mammalian Brain Neurons. *Journal of Biological Chemistry*, **285**, 15048–15055. doi:10.1074/jbc.M109.074260

Kimm, T., Khaliq, Z.M. & Bean, B.P. (2015) Differential Regulation of Action Potential Shape and Burst-Frequency Firing by BK and Kv2 Channels in Substantia Nigra Dopaminergic Neurons. *The Journal of Neuroscience*, **35**, 16404–17. doi:10.1523/JNEUROSCI.5291-14.2015

King, A.N., Manning, C.F. & Trimmer, J.S. (2014) A unique ion channel clustering domain on the axon initial segment of mammalian neurons. *Journal of Comparative Neurology*, **522**, 2594–2608. doi:10.1002/cne.23551

Kirmiz, M., Palacio, S., Thapa, P., King, A.N., Sack, J.T. & Trimmer, J.S. (2018) Remodeling neuronal ER-PM junctions is a conserved nonconducting function of Kv2 plasma membrane ion channels. *Molecular Biology of the Cell*, **29**, 2410–2432. doi:10.1091/mbc.E18-05-0337

Kirmiz, M., Vierra, N.C., Palacio, S. & Trimmer, J.S. (2018) Identification of VAPA and VAPB as Kv2 Channel-Interacting Proteins Defining Endoplasmic Reticulum–Plasma Membrane Junctions in Mammalian Brain Neurons. *The Journal of Neuroscience*, **38**, 7562–7584. doi:10.1523/JNEUROSCI.0893-18.2018

Lee, H.C., Wang, J.M. & Swartz, K.J. (2003) Interaction between extracellular Hanatoxin and the resting conformation of the voltage-sensor paddle in Kv channels. *Neuron*, **40**, 527–36. doi:10.1016/S0896-6273(03)00636-6

Lewis, G.N. (1925) A New Principle of Equilibrium. *Proceedings of the National Academy of Sciences of the United States of America*, **11**, 179–83, National Academy of Sciences. doi:10.1073/pnas.11.3.179

Li, H., Guo, W., Xu, H., Hood, R., Benedict, A.T. & Nerbonne, J.M. (2001) Functional expression of a GFP-tagged Kv1.5 alpha-subunit in mouse ventricle. *American Journal of Physiology. Heart and Circulatory Physiology*, **281**, H1955-67. doi:10.1152/ajpheart.2001.281.5.H1955

Li, X., Liu, H., Chu Luo, J., Rhodes, S.A., Trigg, L.M., Rossum, D.B. van, Anishkin, A., *et al.* (2015) Major diversification of voltage-gated K+ channels occurred in ancestral parahoxozoans. *Proceedings of the National Academy of Sciences of the United States of America*, **112**, E1010-9. doi:10.1073/pnas.1422941112

Lim, S.T., Antonucci, D.E., Scannevin, R.H. & Trimmer, J.S. (2000) A novel targeting signal for proximal clustering of the Kv2.1 K+ channel in hippocampal neurons. *Neuron*, **25**, 385–97. doi:10.1016/S0896-6273(00)80902-2

Lin, M.Z. & Schnitzer, M.J. (2016) Genetically encoded indicators of neuronal activity. *Nature Neuroscience*, **19**, 1142–1153. doi:10.1038/nn.4359

Liu, P.W. & Bean, B.P. (2014) Kv2 channel regulation of action potential repolarization and firing patterns in superior cervical ganglion neurons and hippocampal CA1 pyramidal neurons. *The Journal of Neuroscience*, **34**, 4991–5002. doi:10.1523/JNEUROSCI.1925-13.2014

Long, S.B., Campbell, E.B. & Mackinnon, R. (2005) Voltage Sensor of Kv1.2: Structural Basis of Electromechanical Coupling. *Science*, **309**, 903–908. doi:10.1126/science.1116270

Long, S.B., Tao, X., Campbell, E.B. & MacKinnon, R. (2007) Atomic structure of a voltage-dependent K+ channel in a lipid membrane-like environment. *Nature*, **450**, 376–82. doi:10.1038/nature06265

MacDonald, P.E., Salapatek, A.M.F. & Wheeler, M.B. (2003) Temperature and redox state dependence of native Kv2.1 currents in rat pancreatic beta-cells. *The Journal of Physiology*, **546**, 647–53. doi:10.1113/jphysiol.2002.035709

Maffie, J.K., Dvoretskova, E., Bougis, P.E., Martin-Eauclaire, M.-F. & Rudy, B. (2013) Dipeptidyl-peptidase-like-proteins confer high sensitivity to the scorpion toxin AmmTX3 to Kv4-mediated A-type K+ channels. *The Journal of Physiology*, **591**, 2419–27. doi:10.1113/jphysiol.2012.248831

Mandikian, D., Bocksteins, E., Parajuli, L.K., Bishop, H.I., Cerda, O., Shigemoto, R. & Trimmer, J.S. (2014) Cell type-specific spatial and functional coupling between mammalian brain Kv2.1 K+ channels and ryanodine receptors. *The Journal of Comparative Neurology*, **522**, 3555–74. doi:10.1002/cne.23641

Mann, V.R., Powers, A.S., Tilley, D.C., Sack, J.T. & Cohen, B.E. (2018) Azide-Alkyne Click Conjugation on Quantum Dots by Selective Copper Coordination. *ACS Nano*, **12**, 4469–4477. doi:10.1021/acsnano.8b00575

McCormack, K., Santos, S., Chapman, M.L., Krafte, D.S., Marron, B.E., West, C.W., Krambis, M.J., *et al.* (2013) Voltage sensor interaction site for selective small molecule inhibitors of voltage-gated sodium channels. *Proceedings of the National Academy of Sciences of the United States of America*, **110**, E2724–E2732. doi:10.1073/pnas.1220844110

McDonough, S.I., Mintz, I.M. & Bean, B.P. (1997) Alteration of P-type calcium channel gating by the spider toxin omega-Aga-IVA. *Biophysical Journal*, **72**, 2117–28. doi:10.1016/S0006-3495(97)78854-4

Milescu, M., Bosmans, F., Lee, S., Alabi, A.A., Kim, J. Il & Swartz, K.J. (2009) Interactions between lipids and voltage sensor paddles detected with tarantula toxins. *Nature Structural & Molecular Biology*, **16**, 1080–5. doi:10.1038/nsmb.1679

Misonou, H., Menegola, M., Mohapatra, D.P., Guy, L.K., Park, K.-S. & Trimmer, J.S. (2006) Bidirectional Activity-Dependent Regulation of Neuronal Ion Channel Phosphorylation. *Journal of Neuroscience*, **26**, 13505–13514. doi:10.1523/JNEUROSCI.3970-06.2006

Misonou, H., Mohapatra, D.P., Menegola, M. & Trimmer, J.S. (2005) Calcium- and metabolic state-dependent modulation of the voltage-dependent Kv2.1 channel regulates neuronal excitability in response to ischemia. *The Journal of Neuroscience*, **25**, 11184–93. doi:10.1523/JNEUROSCI.3370-05.2005

Misonou, H., Mohapatra, D.P., Park, E.W., Leung, V., Zhen, D., Misonou, K., Anderson, A.E., *et al.* (2004) Regulation of ion channel localization and phosphorylation by neuronal activity. *Nature Neuroscience*, **7**, 711–718. doi:10.1038/nn1260

Murakoshi, H., Shi, G., Scannevin, R.H. & Trimmer, J.S. (1997) Phosphorylation of the Kv2.1 K+ channel alters voltage-dependent activation. *Molecular Pharmacology*, **52**, 821–8. doi:10.1124/mol.52.5.821

Murakoshi, H. & Trimmer, J.S. (1999) Identification of the Kv2.1 K+ channel as a major component of the delayed rectifier K+ current in rat hippocampal neurons. *The Journal of Neuroscience*, **19**, 1728–35. doi:10.1523/jneurosci.19-05-01728.1999

O'Connell, K.M.S., Loftus, R. & Tamkun, M.M. (2010) Localization-dependent activity of the Kv2.1 delayed-rectifier K+ channel. *Proceedings of the National Academy of Sciences of the United States of America*, **107**, 12351–12356. doi:10.1073/pnas.1003028107

Opitz-Araya, X. & Barria, A. (2011) Organotypic hippocampal slice cultures. *Journal of Visualized Experiments*, MyJoVE Corporation. doi:10.3791/2462

Palacio, S., Chevaleyre, V., Brann, D.H., Murray, K.D., Piskorowski, R.A. & Trimmer, J.S. (2017) Heterogeneity in Kv2 Channel Expression Shapes Action Potential Characteristics and Firing Patterns in CA1 versus CA2 Hippocampal Pyramidal Neurons. *eNeuro*, **4**, ENEURO.0267-17.2017. doi:10.1523/ENEURO.0267-17.2017

Patel, A.J., Lazdunski, M. & Honoré, E. (1997) Kv2.1/Kv9.3, a novel ATP-dependent delayed-rectifier K+ channel in oxygen-sensitive pulmonary artery myocytes. *The EMBO Journal*, **16**, 6615–25. doi:10.1093/emboj/16.22.6615

Pathak, D., Guan, D. & Foehring, R.C. (2016) Roles of specific Kv channel types in repolarization of the action potential in genetically identified subclasses of pyramidal neurons in mouse neocortex. *Journal of Neurophysiology*, **115**, 2317–2329. doi:10.1152/jn.01028.2015

Peltola, M.A., Kuja-Panula, J., Lauri, S.E., Taira, T. & Rauvala, H. (2011) AMIGO is an auxiliary subunit of the Kv2.1 potassium channel. *EMBO Reports*, **12**, 1293–1299. doi:10.1038/embor.2011.204

Peretz, A., Pell, L., Gofman, Y., Haitin, Y., Shamgar, L., Patrich, E., Kornilov, P., *et al.* (2010) Targeting the voltage sensor of Kv7.2 voltage-gated K+ channels with a new gating-modifier. *Proceedings of the National Academy of Sciences of the United States of America*, **107**, 15637–42. doi:10.1073/pnas.0911294107

Plant, L.D., Dowdell, E.J., Dementieva, I.S., Marks, J.D. & Goldstein, S.A.N. (2011) SUMO modification of cell surface Kv2.1 potassium channels regulates the activity of rat hippocampal neurons. *The Journal of General Physiology*, **137**, 441–54. doi:10.1085/jgp.201110604

Pologruto, T.A., Sabatini, B.L. & Svoboda, K. (2003) ScanImage: flexible software for operating laser scanning microscopes. *Biomedical Engineering Online*, **2**, 13. doi:10.1186/1475-925X-2-13

Ramu, Y., Xu, Y. & Lu, Z. (2006) Enzymatic activation of voltage-gated potassium channels. *Nature*, **442**, 696–699. doi:10.1038/nature04880

Redman, P.T., He, K., Hartnett, K.A., Jefferson, B.S., Hu, L., Rosenberg, P.A., Levitan, E.S., *et al.* (2007) Apoptotic surge of potassium currents is mediated by p38 phosphorylation of Kv2.1. *Proceedings of the National Academy of Sciences of the United States of America*, **104**, 3568–73. doi:10.1073/pnas.0610159104

Sack, J.T., Aldrich, R.W. & Gilly, W.F. (2004) A gastropod toxin selectively slows early transitions in the Shaker K channel's activation pathway. *The Journal of General Physiology*, **123**, 685–96. doi:10.1085/jgp.200409047

Sack, J.T., Stephanopoulos, N., Austin, D.C., Francis, M.B. & Trimmer, J.S. (2013) Antibody-guided photoablation of voltage-gated potassium currents. *The Journal of General Physiology*, **142**, 315–24. doi:10.1085/jgp.201311023

Saitsu, H., Akita, T., Tohyama, J., Goldberg-Stern, H., Kobayashi, Y., Cohen, R., Kato, M., *et al.* (2015) De novo KCNB1 mutations in infantile epilepsy inhibit repetitive neuronal firing. *Scientific Reports*, **5**, 15199. doi:10.1038/srep15199

Scannevin, R.H., Murakoshi, H., Rhodes, K.J. & Trimmer, J.S. (1996) Identification of a cytoplasmic domain important in the polarized expression and clustering of the Kv2.1 K+ channel. *The Journal of Cell Biology*, **135**, 1619–32. doi:10.1083/jcb.135.6.1619

Schmalhofer, W.A., Calhoun, J., Burrows, R., Bailey, T., Kohler, M.G., Weinglass, A.B., Kaczorowski, G.J., *et al.* (2008) ProTx-II, a selective inhibitor of NaV1.7 sodium channels, blocks action potential propagation in nociceptors. *Molecular Pharmacology*, **74**, 1476–84. doi:10.1124/mol.108.047670

Schmalhofer, W.A., Ratliff, K.S., Weinglass, A., Kaczorowski, G.J., Garcia, M.L. & Herrington, J. (2009) A KV2.1 gating modifier binding assay suitable for high throughput screening. *Channels*, **3**, 437–47. doi:10.4161/chan.3.6.10201

Schmalz, F., Kinsella, J., Koh, S.D., Vogalis, F., Schneider, A., Flynn, E.R.M., Kenyon, J.L., *et al.* (1998) Molecular identification of a component of delayed rectifier current in gastrointestinal smooth muscles. *American Journal of Physiology-Gastrointestinal and Liver Physiology*, **274**, G901–G911. doi:10.1152/ajpgi.1998.274.5.G901

Schneider, C.A., Rasband, W.S. & Eliceiri, K.W. (2012) NIH Image to ImageJ: 25 years of image analysis. *Nature Methods*, **9**, 671–5. doi:10.1038/nmeth.2089

Schneider, M.F. & Chandler, W.K. (1973) Voltage dependent charge movement of skeletal muscle: a possible step in excitation-contraction coupling. *Nature*, **242**, 244–6. doi:10.1038/242244a0

Scholle, A., Dugarmaa, S., Zimmer, T., Leonhardt, M., Koopmann, R., Engeland, B., Pongs, O., *et al.* (2004) Rate-limiting reactions determining different activation kinetics of Kv1.2 and Kv2.1 channels. *The Journal of Membrane Biology*, **198**, 103–12. doi:10.1007/s00232-004-0664-0

Seoh, S.A., Sigg, D., Papazian, D.M. & Bezanilla, F. (1996) Voltage-sensing residues in the S2 and S4 segments of the Shaker K+ channel. *Neuron*, **16**, 1159–67. doi:10.1016/S0896-6273(00)80142-7

Shi, G., Kleinklaus, A.K., Marrion, N. V & Trimmer, J.S. (1994) Properties of Kv2.1 K+ channels expressed in transfected mammalian cells. *The Journal of Biological Chemistry*, **269**, 23204–11. Retrieved from http://www.ncbi.nlm.nih.gov/pubmed/8083226

Shi, G., Nakahira, K., Hammond, S., Rhodes, K.J., Schechter, L.E. & Trimmer, J.S. (1996) Beta subunits promote K+ channel surface expression through effects early in biosynthesis. *Neuron*, **16**, 843–52. doi:10.1016/S0896-6273(00)80104-X

Shibata, R., Misonou, H., Campomanes, C.R., Anderson, A.E., Schrader, L.A., Doliveira, L.C., Carroll, K.I., *et al.* (2003) A fundamental role for KChIPs in determining the molecular properties and trafficking of Kv4.2 potassium channels. *The Journal of Biological Chemistry*, **278**, 36445–54. doi:10.1074/jbc.M306142200

Speca, D.J., Ogata, G., Mandikian, D., Bishop, H.I., Wiler, S.W., Eum, K., Wenzel, H.J., *et al.* (2014) Deletion of the Kv2.1 delayed rectifier potassium channel leads to neuronal and behavioral hyperexcitability. *Genes, Brain, and Behavior*, **13**, 394–408. doi:10.1111/gbb.12120

Stoppini, L., Buchs, P.A. & Muller, D. (1991) A simple method for organotypic cultures of nervous tissue. *Journal of Neuroscience Methods*, **37**, 173–82. doi:10.1016/0165-0270(91)90128-M

Swartz, K.J. (2007) Tarantula toxins interacting with voltage sensors in potassium channels. *Toxicon*, **49**, 213–30. doi:10.1016/j.toxicon.2006.09.024

Tao, X., Lee, A., Limapichat, W., Dougherty, D.A. & MacKinnon, R. (2010) A Gating Charge Transfer Center in Voltage Sensors. *Science*, **328**, 67–73. doi:10.1126/science.1185954

Thiffault, I., Speca, D.J., Austin, D.C., Cobb, M.M., Eum, K.S., Safina, N.P., Grote, L., *et al.* (2015) A novel epileptic encephalopathy mutation in KCNB1 disrupts Kv2.1 ion selectivity, expression, and localization. *The Journal of General Physiology*, **146**, 399–410. doi:10.1085/jgp.201511444

Tilley, D.C., Angueyra, J.M., Eum, K.S., Kim, H., Chao, L.H., Peng, A.W. & Sack, J.T. (2019) The tarantula toxin GxTx detains K+ channel gating charges in their resting conformation. *The Journal of General Physiology*, **151**, 292–315. doi:10.1085/jgp.201812213

Tilley, D.C., Eum, K.S., Fletcher-Taylor, S., Austin, D.C., Dupre, C., Patron, L.A., Garcia, R.L., *et al.* (2014) Chemoselective tarantula toxins report voltage activation of wild-type ion channels in live cells. *Proceedings of the National Academy of Sciences of the United States of America*, **111**, E4789-96. doi:10.1073/pnas.1406876111

Torkamani, A., Bersell, K., Jorge, B.S., Bjork, R.L., Friedman, J.R., Bloss, C.S., Cohen, J., *et al.* (2014) De novo *KCNB1* mutations in epileptic encephalopathy. *Annals of Neurology*, **76**, 529–540. doi:10.1002/ana.24263

Trapani, J.G. & Korn, S.J. (2003) Control of ion channel expression for patch clamp recordings using an inducible expression system in mammalian cell lines. *BMC Neuroscience*, **4**, 15. doi:10.1186/1471-2202-4-15

Trimmer, J.S. (1991) Immunological identification and characterization of a delayed rectifier K+ channel polypeptide in rat brain. *Proceedings of the National Academy of Sciences of the United States of America*, **88**, 10764–8. doi:10.1073/pnas.88.23.10764

Trimmer, J.S. (2015) Subcellular localization of K+ channels in mammalian brain neurons: remarkable precision in the midst of extraordinary complexity. *Neuron*, **85**, 238–56. doi:10.1016/j.neuron.2014.12.042

Tsvetanova, N.G., Irannejad, R. & Zastrow, M. von. (2015) G Protein-coupled Receptor (GPCR) Signaling via Heterotrimeric G Proteins from Endosomes. *Journal of Biological Chemistry*, **290**, 6689–6696. doi:10.1074/jbc.R114.617951

Woods, G. & Zito, K. (2008) Preparation of gene gun bullets and biolistic transfection of neurons in slice culture. *Journal of Visualized Experiments*, pii:675. doi:10.3791/675

Wu, X., Hernandez-Enriquez, B., Banas, M., Xu, R. & Sesti, F. (2013) Molecular mechanisms underlying the apoptotic effect of KCNB1 K+ channel oxidation. *The Journal of Biological Chemistry*, **288**, 4128–34. doi:10.1074/jbc.M112.440933

Xia, X.M., Ding, J.P. & Lingle, C.J. (1999) Molecular basis for the inactivation of Ca2+- and voltage-dependent BK channels in adrenal chromaffin cells and rat insulinoma tumor cells. *The Journal of Neuroscience*, **19**, 5255–64. doi:10.1523/jneurosci.19-13-05255.1999

Xu, H., Li, T., Rohou, A., Arthur, C.P., Tzakoniati, F., Wong, E., Estevez, A., *et al.* (2019) Structural Basis of Nav1.7 Inhibition by a Gating-Modifier Spider Toxin. *Cell*, **176**, 1238–1239. doi:10.1016/j.cell.2019.01.047

Xu, Y., Ramu, Y. & Lu, Z. (2008) Removal of phospho-head groups of membrane lipids immobilizes voltage sensors of K+ channels. *Nature*, **451**, 826–829. doi:10.1038/nature06618

Yang, F. & Zheng, J. (2014) High temperature sensitivity is intrinsic to voltage-gated potassium channels. *eLife*, **3**, e03255. doi:10.7554/eLife.03255

Yang, W. & Yuste, R. (2017) In vivo imaging of neural activity. *Nature Methods*, **14**, 349–359. doi:10.1038/nmeth.4230

Yazulla, S. & Studholme, K.M. (1998) Differential distribution of Shaker-like and Shab-like K+-channel subunits in goldfish retina and retinal bipolar cells. *The Journal of Comparative Neurology*, **396**, 131–40. doi:10.1002/(SICI)1096-9861(19980622)396

Zagotta, W.N., Hoshi, T., Dittman, J. & Aldrich, R.W. (1994) Shaker potassium channel gating. II: Transitions in the activation pathway. *The Journal of General Physiology*, **103**, 279–319. doi:10.1085/jgp.103.2.279

Zhang, A.H., Sharma, G., Undheim, E.A.B., Jia, X. & Mobli, M. (2018) A complicated complex: Ion channels, voltage sensing, cell membranes and peptide inhibitors. *Neuroscience Letters*, **679**, 35–47. doi:10.1016/j.neulet.2018.04.030

Zhang, G., Zheng, S., Liu, H. & Chen, P.R. (2015) Illuminating biological processes through site-specific protein labeling. *Chemical Society Reviews*, **44**, 3405–3417. doi:10.1039/C4CS00393D

Zhang, Y., McKay, S.E., Bewley, B. & Kaczmarek, L.K. (2008) Repetitive firing triggers clustering of Kv2.1 potassium channels in Aplysia neurons. *The Journal of Biological Chemistry*, **283**, 10632–41. doi:10.1074/jbc.M800253200

Zheng, J. & Trudeau, M.C. (2016) *Handbook of Ion Channels*. (J. Zheng & M. C. Trudeau, Eds.), CRC Press.

Zheng, Y., Liu, P., Bai, L., Trimmer, J.S., Bean, B.P. & Ginty, D.D. (2019) Deep Sequencing of Somatosensory Neurons Reveals Molecular Determinants of Intrinsic Physiological Properties. *Neuron*. doi:10.1016/j.neuron.2019.05.039

**Figure Legends**

Figure 1: ***GxTX-594 colocalizes with Kv2-GFP channels.***

A. Fluorescence a CHO cells transfected with Kv2.1-GFP (Top) or Kv2.2-GFP (Bottom) and labeled with GxTX-594. Optical sections were near the glass-adhered cell surface. Cells were incubated with 100 nM GxTX-594 for 5 minutes and rinsed before imaging. Fluorescence shown corresponds to emission of GFP (Left), Alexa 594 (Middle), or an overlay of GFP and Alexa 594 channels (Right). Scale bars are 20 µm.
B. Pearson correlation coefficient for GxTX-594 colocalization with Kv2.1-GFP or Kv2.2-GFP (Top). Ratio of magenta to green intensity between GxTX-594 and Kv2-GFP (Bottom). Circles indicate measurements from individual cells. Pixel intensities were background subtracted before analyses by subtracting the average fluorescence of a background ROI that did not contain cells from the ROI containing the cell. All data from the same application of GxTX-594. Bars are arithmetic mean.

Figure 1 Supplement 1: ***Synthesis of GxTX-594.***

A. Molecular model of Alexa 594-maleimide conjugated to the spinster thiol of GxTX-Cys13. Scale bar is 10 angstroms.
B. HPLC chromatogram of GxTX-Cys13. Gradient described in *Methods*. GxTX-Cys13 eluted at 12.6 minutes, peak 1, which corresponds to 33% acetonitrile. MALDI-TOF MS profile of peak 1 (Inset). Rel. Int. is Relative Intensity.
C. HPLC profile of GxTX-594 conjugation reaction between Alexa 594-maleimide and GxTX-Cys13. Peak 1 is GxTX-Cys13 (Retention time: 12.8 minutes, 33% acetonitrile), peak 2 is a minor product from conjugation, and peak 3 is the major product from conjugation (Retention time: 16.4 minutes, 35% acetonitrile). The fractions corresponding to peak 3 were combined.
D. HPLC chromatogram profile of GxTX-594. 2 µL of 13.1 µM GxTX-594 diluted in 200 µL of 0.1 % TFA was injected. MALDI-TOF MS profile of GxTX-594 (Inset).

Figure 2: ***GxTX-594 is selective for Kv2 channels.***

A. Fluorescence from live CHO cells transfected with Kv2.1-GFP, Kv2.2-GFP, Kv4.2-GFP + KChIP2, Kv1.5-GFP + Kvβ2, or BK-GFP (Indicated by row) and labeled with GxTX-594. Airy disk imaging was from a plane above the glass-adhered surface. Cells were incubated with 100 nM GxTX-594 and 5 μg/mL WGA-405 then rinsed before imaging. Fluorescence shown corresponds to emission of GFP (Column 1), Alexa 594 (Column 2), WGA-405 (Column 3), or an overlay of GFP, Alexa 594, and WGA-405 channels (Column 4). Scale bars are 20 μm.
B. GxTX-594:GFP fluorescence intensity ratios for different $K^+$ channel-GFP types. Values were normalized to the average GxTX-594:Kv2.1-GFP ratio. Circles indicate measurements from individual cells. Only cells with obvious GFP expression were analyzed. For analysis ROIs were drawn around the cell membrane indicated by WGA-405 fluorescence. Pixel intensities were background-subtracted before analyses by subtracting the average fluorescence of a background ROI that did not contain cells from the ROI containing the cell, this occasionally resulted in ROIs with negative intensity. Kv2.1 n = 16, Kv2.2 n = 10, Kv4.2 n = 13, Kv1.5 n = 13, BK n =10; n indicates the number of individual cells analyzed during a single application of GxTX-594. Bars are arithmetic mean. Significant differences were observed between GxTX:GFP ratio for Kv2.1 or Kv2.2 and Kv1.5, Kv4.2, or BK by Mann-Whitney ($p<0.0001$).
C. Pearson correlation coefficients between GxTX-594 and GFP. Same cells as panel B. Significant differences were observed between correlation coefficients for Kv2.1 or Kv2.2 and Kv1.5, Kv4.2, or BK by Mann-Whitney ($p<0.0001$).

Figure 2 Supplement 1: ***GxTX-594 colocalizes with Kv2 ion channels.***

A. Exemplar whole-cell voltage clamp recordings of CHO cells expressing Kv2.1-GFP, Kv2.2-GFP, Kv4.2-GFP, Kv1.5-GFP, or BK-GFP (Indicated by row in panel B). Recordings shown are representative responses to 100 ms steps from -100 mV to -40, 0 and +40 mV.
B. Fluorescence from live CHO cells transfected with Kv2.1-GFP, Kv2.2-GFP, Kv4.2-GFP Kv1.5-GFP, or BK-GFP (Indicated by row) and labeled with GxTX-594. Confocal imaging plane was above the glass-adhered surface. Cells were incubated with 100 nM GxTX-594 and 5 µg/mL WGA-405 and rinsed before imaging. Fluorescence shown corresponds to emission of GFP (Column 1), Alexa 594 (Column 2), WGA-405 (Column 3), or an overlay of GFP, Alexa 594, and WGA-405 channels (Column 4). Scale bars are 20 µm.
C. Background-subtracted GxTX-594:GFP ratio for different GFP and $K^+$ channel subtypes normalized to the average GxTX-594:Kv2.1-GFP ratio. Analysis same as in Figure 2 B. Kv2.1 n = 11, Kv2.2 n = 9, Kv4.2 n = 13, Kv1.5 = 13, and BK n =12. Cells were compiled from two independent GxTX-594 applications, each circle corresponds to a cell. Significant differences were observed between GxTX:GFP ratio for Kv2.1 or Kv2.2 and Kv1.5, Kv4.2, or BK by Mann-Whitney ($p<0.0001$).
D. Pearson correlation coefficients between GxTX-594 and GFP. Unless otherwise noted analysis was same as in Figure 2 C. Same cells as panel C.

Figure 3: ***GxTX594 binds Kv2.1 in the presence of its auxiliary subunit AMIGO-1.***

A. Fluorescence from Kv2.1-CHO cells transfected with AMIGO-1-YFP. Imaging plane was near the glass-adhered cell surface. Cells were incubated in indicated concentrations of GxTX-594 for 15 minutes then washed out before imaging. Fluorescence shown corresponds to YFP (Green) and Alexa 594 (Magenta). Scale bar is 20 µm. Yellow line is a representative AMIGO-1 positive ROI.
B. Pearson correlation coefficient between AMIGO-1-YFP and GxTX-594 within AMIGO positive ROIs. Coefficients from 1000 nM dose of GxTX-594. n = 8 ROIs total over 3 independent experiments. Bar is arithmetic mean.
C. Time-lapse GxTX-594 fluorescence intensity from the dose-response experiment shown in A. The gray trace represents AMIGO-1-YFP positive cells, black trace represents AMIGO-1-YFP negative cells. Fluorescence was not background-subtracted. $F_{max}$ is intensity while cells were incubated in 1000 nM GxTX-594.
D. Changes in fluorescence were analyzed at each concentration from multiple dose response experiments. Hollow markers correspond to 3 independent experiments. Lines are fit of a Langmuir isotherm (Hill equation with slope held at 1) to obtain a dissociation constant ($K_d$) for GxTX-594; AMIGO-1-YFP positive $K_d$ = 26.7 nM ± 14.3; AMIGO-1-YFP negative $K_d$ = 26.9 nM ± 8.3.

Figure 4: ***GxTX-594 labeling responds to transmembrane voltage.***

A. Fluorescence intensities from an optical section of a voltage-clamped Kv2.1- CHO cell in 9 nM GxTX-594. Pseudocolored images indicate maximal intensities in white. Rows indicate voltage step taken from a holding potential of -80 mV. Columns indicate time after voltage step. Scale bar is 10 µm.

B. GxTX-594 fluorescence during steps to indicated voltages. Smooth lines are fits of monoexponential (Eq. 1): -40 mV $k_{\Delta F}$ = 2.2 x $10^{-2}$ ± 2.2 x $10^{-3}$ $s^{-1}$: 0 mV $k_{\Delta F}$ = 1.3 x $10^{-1}$ ± 2.3 x $10^{-3}$ $s^{-1}$, 40 mV $k_{\Delta F}$ = 2.6 x $10^{-1}$ ± 6.2 x $10^{-3}$ $s^{-1}$ and 80 mV $k_{\Delta F}$ = 5.3 x $10^{-1}$ ± 1.1 x $10^{-2}$ $s^{-1}$. ROIs were hand-drawn around the apparent cell surface membrane based on GxTX-594 fluorescence. Background for subtraction was the average intensity of a region that did not contain cells over the time course of the voltage protocol. Each trace was normalized to initial fluorescence intensity before the application of the voltage stimulus.

C. Fluorescence intensity remaining at the end of 50 s +80 mV steps. Each circle represents one cell. Background subtraction and normalization as in panel B.

D. Voltage-dependence of fluorescence intensity at the end of 50 s steps. Data normalized to 100% for -80 mV and 0% for +80 mV. Circle coloring indicates data from the same cell. Gray circles represent data shown in B. Black line is fit of a first-order Boltzmann equation as in Tilley et al., 2019: $V_{1/2}$ = -27.4 ± 2.5 mV, $z$ = -1.38 ± 0.13 $e_0$. Blue line is prediction from Scheme I at 9 nM GxTX. Bars are arithmetic mean ± standard error.

E. Voltage dependence of fluorescence intensity kinetics at end of 50 s steps. Circle coloring is the same as panel D. Black line is a first-order Boltzmann equation fit to the logarithm of $k_{\Delta F}$: $V_{1/2}$ = 2.3 ± 7.9 mV, $z$ = 1.14 ± 0.38 $e_0$. Blue line is prediction from Scheme I at 9 nM GxTX. Bars are geometric mean ± standard error.

Figure 4 Supplement 1: ***GxTX-594 kinetics are impacted by spatially restricted regions.***

A. Airy disk image of the glass adhered surface of a voltage-clamped Kv2.1-CHO cell in 9 nM GxTX-594. Yellow lines indicate boundaries of ROIs. ROI 1, 2, and 3 are concentric circles each with a respective diameter of 1.8, 4.9, and 9.1 µm. ROI 4 was hand-drawn to contain the apparent cell surface. In all cells analyzed, ROI 1-3 were concentric circles of the same sizes, while ROI 4 varied based on cell shape. Scale bar is 10 µm.
B. Representative traces of GxTX-594 fluorescence intensity response to voltage changes. Red lines are monoexponential fits (Eq. 1): 40 mV step ROI 1 $k_{\Delta F} = 4.3 \times 10^{-2} \pm 2.6 \times 10^{-3}$ $s^{-1}$, ROI 2 $k_{\Delta F} = 4.4 \times 10^{-2} \pm 1.6 \times 10^{-3}$ $s^{-1}$, ROI 3 $k_{\Delta F} = 5.7 \times 10^{-2} \pm 1.5 \times 10^{-3}$ $s^{-1}$, ROI 4 $k_{\Delta F} = 9.7 \times 10^{-2} \pm 3.3 \times 10^{-3}$ $s^{-1}$. -80 mV step ROI 1 $k_{\Delta F} = 4.3 \times 10^{-4} \pm 1.1 \times 10^{-5}$ $s^{-1}$, ROI 2 $k_{\Delta F} = 7.9 \times 10^{-4} \pm 5.3 \times 10^{-6}$ $s^{-1}$, ROI 3 $k_{\Delta F} = 2.8 \times 10^{-3} \pm 7.4 \times 10^{-6}$ $s^{-1}$, and ROI 4 $k_{\Delta F} = 5.5 \times 10^{-3} \pm 1.3 \times 10^{-4}$ $s^{-1}$. Background for subtraction was the average intensity of a region that did not contain cells over the time course of the voltage protocol. Each trace was normalized to initial fluorescence intensity before the application of the voltage stimulus.
C. Circles indicate $k_{\Delta F}$ at 40 mV from individual cells. Circle coloring indicates data from the same cell.
D. Circles indicate $k_{\Delta F}$ at -80 mV from individual cells. Circle coloring indicates data from the same cell.

Figure 4 Supplement 2: ***Temperature dependence of GxTX-594 on Kv2.1 CHO cells.***

A. Representative traces of GxTX-594 fluorescence intensity response to voltage changes at 27 °C (black) and 37 °C (gray). Smooth lines are fits of a monoexponential function (Eq. 1): 27 °C $k_{\Delta F}$ = 2.8 x $10^{-2}$ ± 3.9 x $10^{-3}$ $s^{-1}$; 37 °C $k_{\Delta F}$ = 7.5 x $10^{-2}$ ± 5.4 x $10^{-3}$ $s^{-1}$. Background was determined by taking the average fluorescence of a region that did not contain cells over the time course of the voltage protocol. This average was subtracted from each experimental group. Traces were normalized to initial fluorescence intensity before the application of the voltage stimulus.

B. $k_{\Delta F}$ at 27 °C and 37 °C. The rate of fluorescence change was significantly faster at higher temperatures (Mann-Whitney p = 0.0005). From geometric means (Bars), a $Q_{10}$ of 3.8 was calculated between 27 °C and 37 °C. Each circle represents one cell, n = 7 both groups.

Figure 5: ***Frequency dependence of GxTX-594 response***

A. Fluorescence intensity on Kv2.1-expressing CHO cells incubated in 9 nM GxTX-594. GxTX-594 fluorescence before frequency stimulus (Left), after 50 s of 200 Hz stimulus (Middle), and 100 s after the cell is returned to resting potential of -80 mV (Right). Note that in each panel the unpatched cell (Left cell in each panel) does not show a change in fluorescence. Scale bar is 10 µm.

B. Representative trace for GxTX-594 unlabeling at 200 Hz. The trace was fit using a monoexponential (Eq. 1). Fit is overlaid and is in red. The $k_{\Delta F}$ at 200 Hz was obtained from this fit. For 200 Hz $k_{\Delta F} = 2.23 \times 10^{-1} \pm 9.9 \times 10^{-3}$ $s^{-1}$. ROIs were hand drawn capturing the cell membrane based on GxTX-594 fluorescence such that only the cell membrane was selected without selecting the dark intracellular region. Background was determined by taking the average fluorescence of a region that did not contain cells over the time course of the protocol. This average was subtracted from each experimental group. Traces were normalized to initial fluorescence intensity before the application of the frequency stimulus.

C. Decrease in fluorescence with increasing stimulus frequency. Circles indicate $F/F_{init}$ from individual cells when stepped to +40 mV at indicated frequencies from a holding potential of -80 mV. Circle coloring indicates data from the same cell. Data normalized to 100% for -80 mV before frequency pulse. Black line is fit of a first-order Boltzmann equation as in Tilley et al., 2019: $V_{1/2} = -0.35 \pm 0.03$ mV, $z = 51.23 \pm 5.19$ $e_0$. Blue line represents decreases in fluorescence at increasing voltages derived from the model shown in Scheme I at a concentration of 9 nM. Bars are arithmetic mean ± standard error.

D. Increases in $k_{\Delta F}$ with increasing stimulus frequency. Rates were obtained from fitting decreases in fluorescence with a monoexponential (Eq. 1) as shown in B. Blue line represents the rates of fluorescence change at increasing frequencies derived from the model shown in Scheme I at a concentration of 9 nM. Bars are geometric mean ± standard error.

Figure 6: ***Relationship of GxTX-594 labeling to probability of channel activation.***

A. Scheme I model predictions of concentration- and voltage-dependence of cell surface fluorescence intensity. Bottom axis represents membrane voltage while the top axis represents the ratio of active to resting voltage sensors for unlabeled Kv2.1. Dashed black line represents the probability that voltage sensors are at rest for unlabeled Kv2.1.
B. Scheme I model predictions of concentration- and voltage-dependence of $k_{\Delta F}$. Colors correspond to panel A.

Figure 7: **GxTX-594 labels CA1 hippocampal pyramidal neurons transfected with Kv2.1-GFP.**

A. Two-photon image of the soma and proximal dendrites of a rat CA1 hippocampal pyramidal neuron in a brain slice six days after transfection with Kv2.1-GFP (Left), labeled with 100 nM GxTX-594 (Middle) and overlay (Right). Image represents a z-projection of 20 optical sections. Scale bar 10 µm.
B. A single optical section of the two-photon image shown in A. GxTX-594 labels both Kv2.1-GFP puncta from a transfected cell and apparent endogenous Kv2 channels from an untransfected cell in the same cultured slice (Right, arrow).
C. Pearson correlation coefficients from CA1 hippocampal neurons two, four, and six days after transfection with Kv2.1-GFP. Each circle represents a different neuron. Bars are arithmetic means.

Figure 7 Supplement 1: **GxTX-594 labels CA1 hippocampal pyramidal neurons transfected with Kv2.1-GFP.**

Two-photon images of Kv2.1-GFP and GxTX-594 on the soma and proximal dendrites of rat CA1 hippocampal pyramidal neurons in brain slices at varying days after transfection with Kv2.1-GFP (Left), labeled with 100 nM (Middle) and overlay (Right). Scale bars 10 µm.

A. Two days after transfection.
B. Four days after transfection.
C. Six days after transfection.

Figure 8: **GxTX-594 puncta on hippocampal CA1 neurons are sensitive to voltage stimulus**

A. Single optical section of fluorescence from CA1 pyramidal neurons in a cultured hippocampal slice after incubation with 100 nM GxTX-594. Scale bar is 5 µm.
B. GxTX-594 fluorescence from a single two-photon optical section before and during depolarization of a whole cell patch-clamped neuron. Text labels of holding potential (-70 mV or 0 mV) indicate approximate position of the patch-clamp pipette. Red arrows indicate stimulus-sensitive puncta, white arrows indicate stimulus-insensitive puncta. Left panel is the average fluorescence of the three frames at -70 mV before depolarization while the right panel is the average fluorescence of three frames after holding potential was stepped to 0 mV. Scale bar is 5 µm. Supplementary Movie 1 contains time-lapse images from this experiment.
C. ROIs used in analysis for panels D, E, and F. Same slice as panel B. ROI 1 contains the apparent plasma membrane of the cell body of the patch-clamped neuron, it was generated by drawing a path tracing the apparent plasma membrane and then expanding to an ROI containing 15 pixels on either side of the path (1.2 µm total width). ROI 2 contains the area 15-45 pixels outside the membrane path (1.2 µm total width). RO1 3 contains the area more than 45 pixels outside of the membrane path. ROI 0 contains the area more than 15 pixels inside the membrane path. Scale bar is 5 µm.
D. Fluorescence from each ROI shown in C. Squares represent ROI 0, circles represent ROI 1, upward triangles represent ROI 2 and upside-down triangles represent ROI 3. 0% $F/F_{init}$ (background) was defined as the mean fluorescence of ROI 0 during the experiment. 100% $F/F_{init}$ was defined as the mean fluorescence of ROI 1 during the first six frames, after subtraction of background. Dotted lines represent the average fluorescence of the first six frames of each ROI. The voltage protocol is shown above.
E. Change in fluorescence during a 0 mV step for different ROIs in multiple hippocampal slices. ROIs for each slice were defined by methods described in panel C. Circles represent mean fluorescence from six frames during 0 mV stimulus, normalized to mean fluorescence from same ROI in six frames before stimulus. Circle color is consistent between ROIs for each hippocampal slice, red circles are from the slice shown in panel D. Black bars are arithmetic mean ± standard error from 3 hippocampal slices.

F. Kinetics of fluorescence change from ROI 1 during a 0 mV step in multiple hippocampal slices. ROI 1 for each slice was defined by the method described in panel C. Lines are monoexponential fits (Eq.1). $k_{\Delta F}$ = 6.8 x $10^{-2}$ ± 2.6 x $10^{-2}$ $s^{-1}$ (yellow), 6.8 x $10^{-2}$ ± 4.6 x $10^{-2}$ $s^{-1}$ (red), and 4.9 x $10^{-2}$ ± 2.1 x $10^{-2}$ $s^{-1}$ (green). The voltage protocol is shown above. Colors of individual circles indicate the same slices as panel E.

G. Region of interest used in analysis for panels H, I, and J. Same image as panel C. The shaded ROI was generated by drawing a path tracing the apparent plasma membrane and then expanding to an ROI containing 5 pixels on either side of the path (0.4 µm total width). Numbers indicate puncta that appear as peaks in panel H. Scale bar is 5 µm.

H. A plot of the fluorescence intensity along the ROI shown in panel G before (red trace) and during (black trace) 0 mV stimulus. Numbers above peaks correspond to puncta labeled in panel G. Red trace: mean fluorescence intensity during the three frames immediately before the stimulus, normalized to mean intensity of entire ROI (black dotted line), plotted against distance along path. Black trace: mean fluorescence intensity during three frames at 0 mV, normalized by the same $F/F_{init}$ value as the red trace.

I. Kinetics of fluorescence change of individual puncta from panel G. Puncta intensity are average intensity of points extending to half maxima of each peak in panel H. Asterisks indicate mean fluorescence intensity of puncta 1 (pink), 4 (red), and 5 (dark red). Lines are monoexponential fits (Eq.1). $k_{\Delta F}$ = 7.1 x $10^{-2}$ ± 2.9 x $10^{-2}$ $s^{-1}$ (pink), 6.7 x $10^{-2}$ ± 2.5 x $10^{-2}$ $s^{-1}$ (red) and 1.2 x $10^{-1}$ ± 5.6 x $10^{-2}$ $s^{-1}$ (dark red). Fits to other puncta had standard deviations larger than $k_{\Delta F}$ values, and were excluded. 100% $F/F_{init}$ was defined as the mean background subtracted fluorescence of the puncta during the six frames before stimuli. The voltage protocol is displayed above. Blue line is prediction from Scheme I.

J. Comparison of fluorescence change of puncta and inter-puncta regions in response to 0 mV stimulus. The regions before stimulus shown in the red line of panel H that had $F/F_{init} \geq 1$ (above average) were binned separately from regions with $F/F_{init} < 1$. The mean fluorescence of each region during 0 mV stimulus (panel H black trace) was compared to the fluorescence before stimulus (panel H red trace). Circles indicate values from three independent hippocampal slices, colors indicate same slices as panel E and F. Black bars are arithmetic mean ± standard error.

K. Rate of fluorescence change of GxTX-594 after a 0 mV stimulus from puncta (as in panel I), ROI 1 (as in panel F) or Kv2.1-CHO cells in 100 nM GxTX-594. Kv2.1-CHO cells were imaged at the same temperature as neurons (30 °C) using neuronal intracellular solution. Normal CHO extracellular solution (CE) was used for Kv2.1-CHO cell experiments. Kv2.1-CHO measurements were made by airy disk confocal imaging. Black bars are mean ± SEM from data shown. Dashed blue line is $k_{\Delta F} = 6.31 \times 10^{-2}\ s^{-1}$ prediction of Scheme I.

**Table 1**

Parameters used for calculations with Scheme I Model

| Parameter | Value |
|---|---|
| $k_{on,resting}$ | 0.003 $s^{-1}$ |
| $k_{off,resting}$ | 0.008 $s^{-1}$ |
| $k_{on,active}$ | 0.002 $s^{-1}$ |
| $k_{off,active}$ | 0.386 $s^{-1}$ |
| $V_{1/2,unlabled}$ | -31.6 mV |
| $V_{1/2,labled}$ | 41.3 mV |
| $z$ | 1.5 $e_0$ |

Figure 1

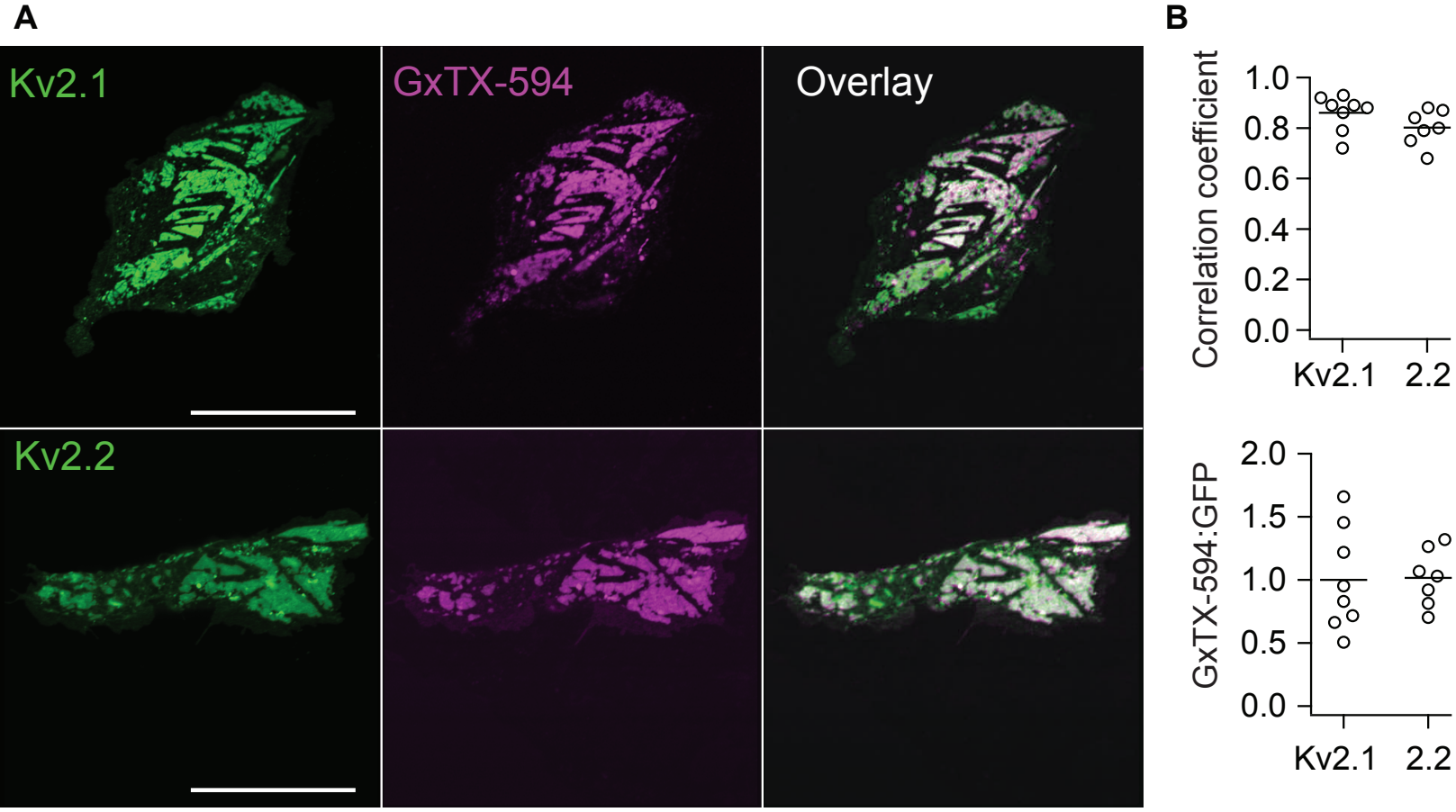
A
Kv2.1
GxTX-594
Overlay
Kv2.2
B
Correlation coefficient
1.0
0.8
0.6
0.4
0.2
0.0
Kv2.1
2.2
GxTX-594:GFP
2.0
1.5
1.0
0.5
0.0
Kv2.1
2.2

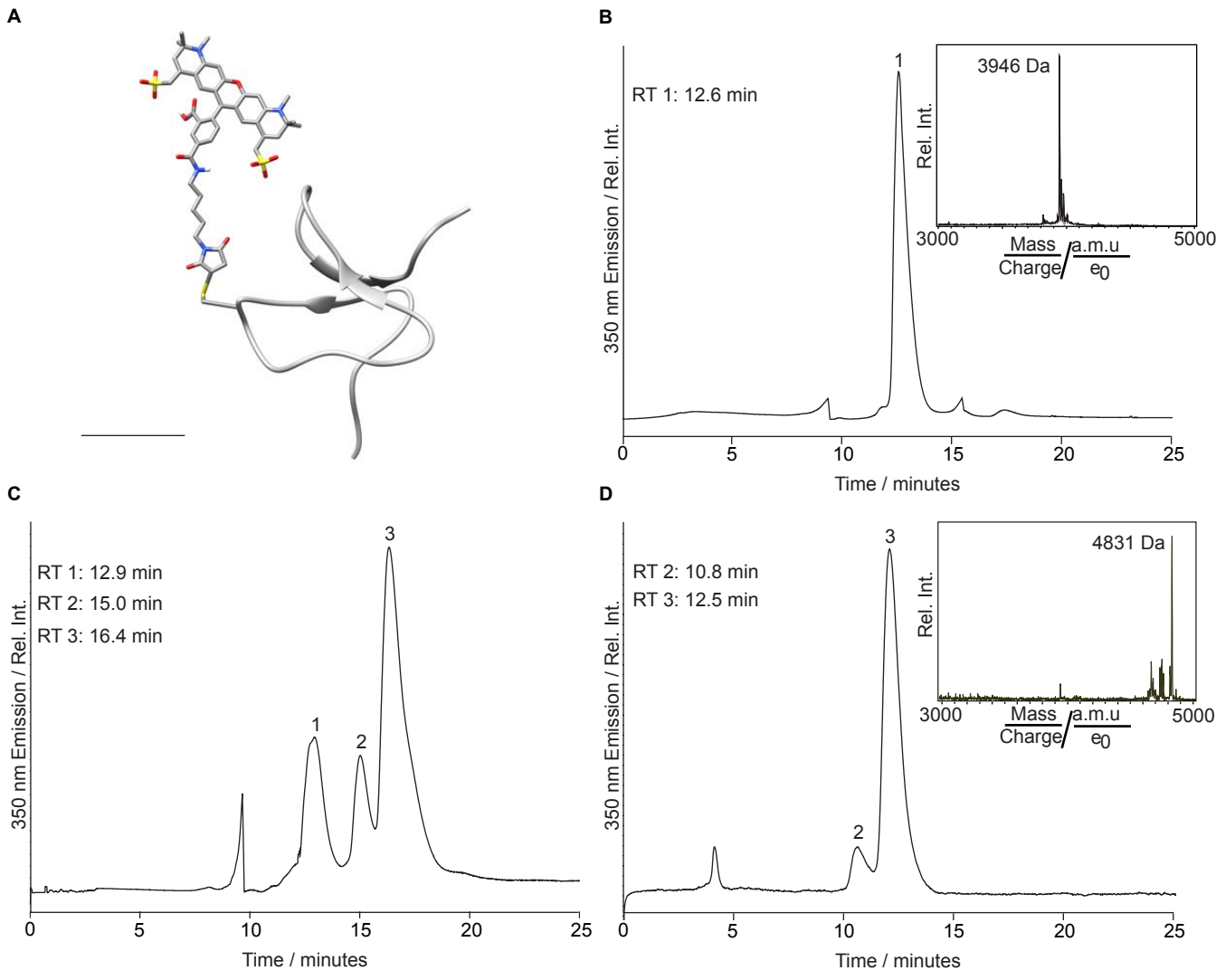
A
B
RT 1: 12.6 min
1
3946 Da
Rel. Int.
3000
5000
Mass / Charge
a.m.u / e0
350 nm Emission / Rel. Int.
0
5
10
15
20
25
Time / minutes
C
RT 1: 12.9 min
RT 2: 15.0 min
RT 3: 16.4 min
1
2
3
350 nm Emission / Rel. Int.
Time / minutes
D
RT 2: 10.8 min
RT 3: 12.5 min
2
3
4831 Da
Rel. Int.
3000
5000
Mass / Charge
a.m.u / e0
350 nm Emission / Rel. Int.
Time / minutes

Figure 2

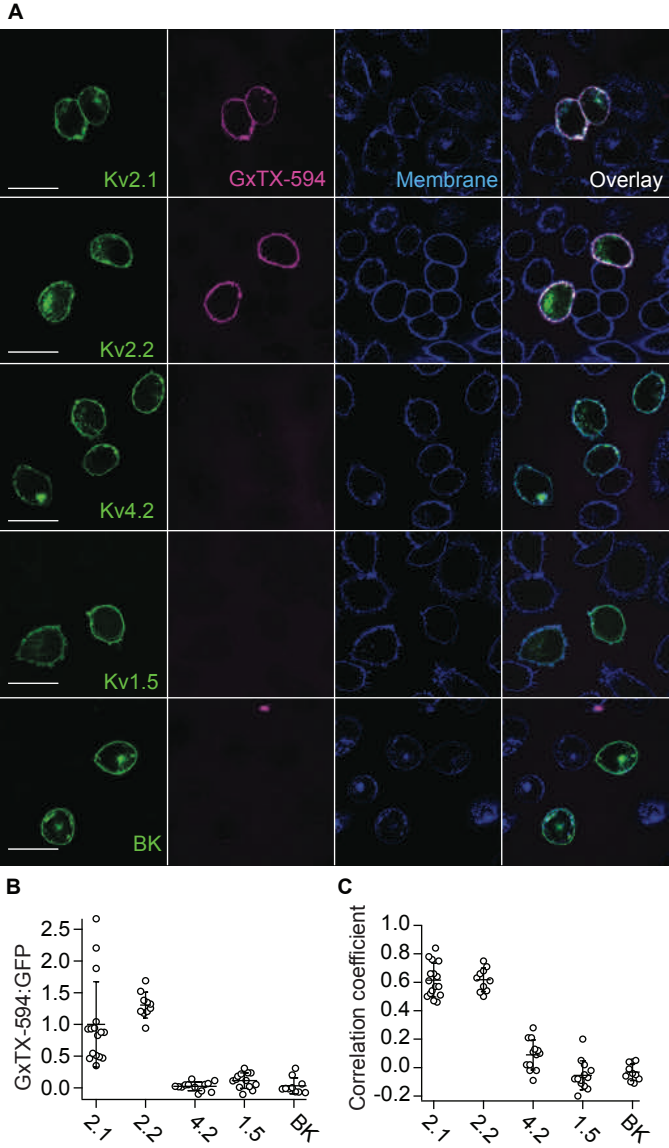
A
Kv2.1
GxTX-594
Membrane
Overlay
Kv2.2
Kv4.2
Kv1.5
BK
B
GxTX-594:GFP
2.5
2.0
1.5
1.0
0.5
0.0
2.1
2.2
4.2
1.5
BK
C
Correlation coefficient
1.0
0.8
0.6
0.4
0.2
0.0
-0.2
2.1
2.2
4.2
1.5
BK

**Figure 2 Supplement 1**

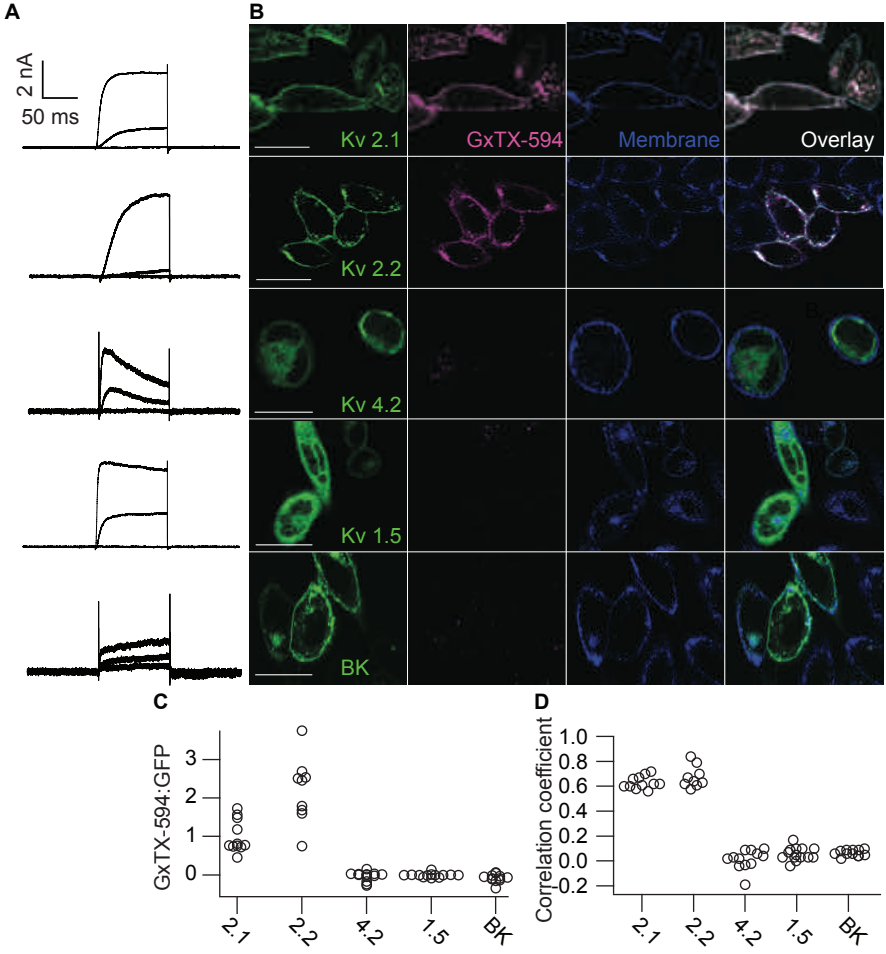

Figure 3

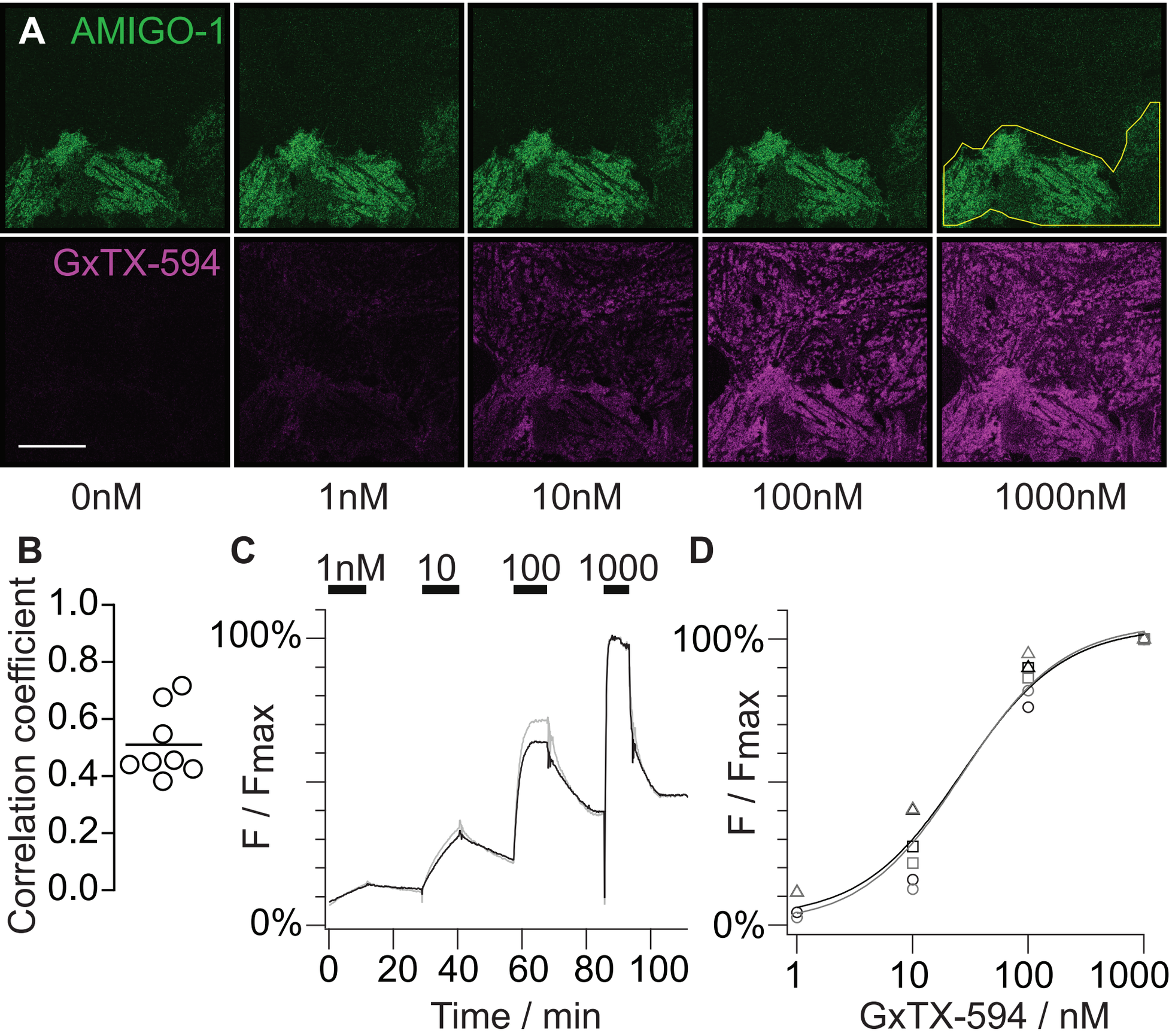
A
AMIGO-1
GxTX-594
0nM
1nM
10nM
100nM
1000nM
B
Correlation coefficient
1.0
0.8
0.6
0.4
0.2
0.0
C
1nM
10
100
1000
100%
0%
F / Fmax
0
20
40
60
80
100
Time / min
D
100%
0%
F / Fmax
1
10
100
1000
GxTX-594 / nM

Figure 4 Supplement 1

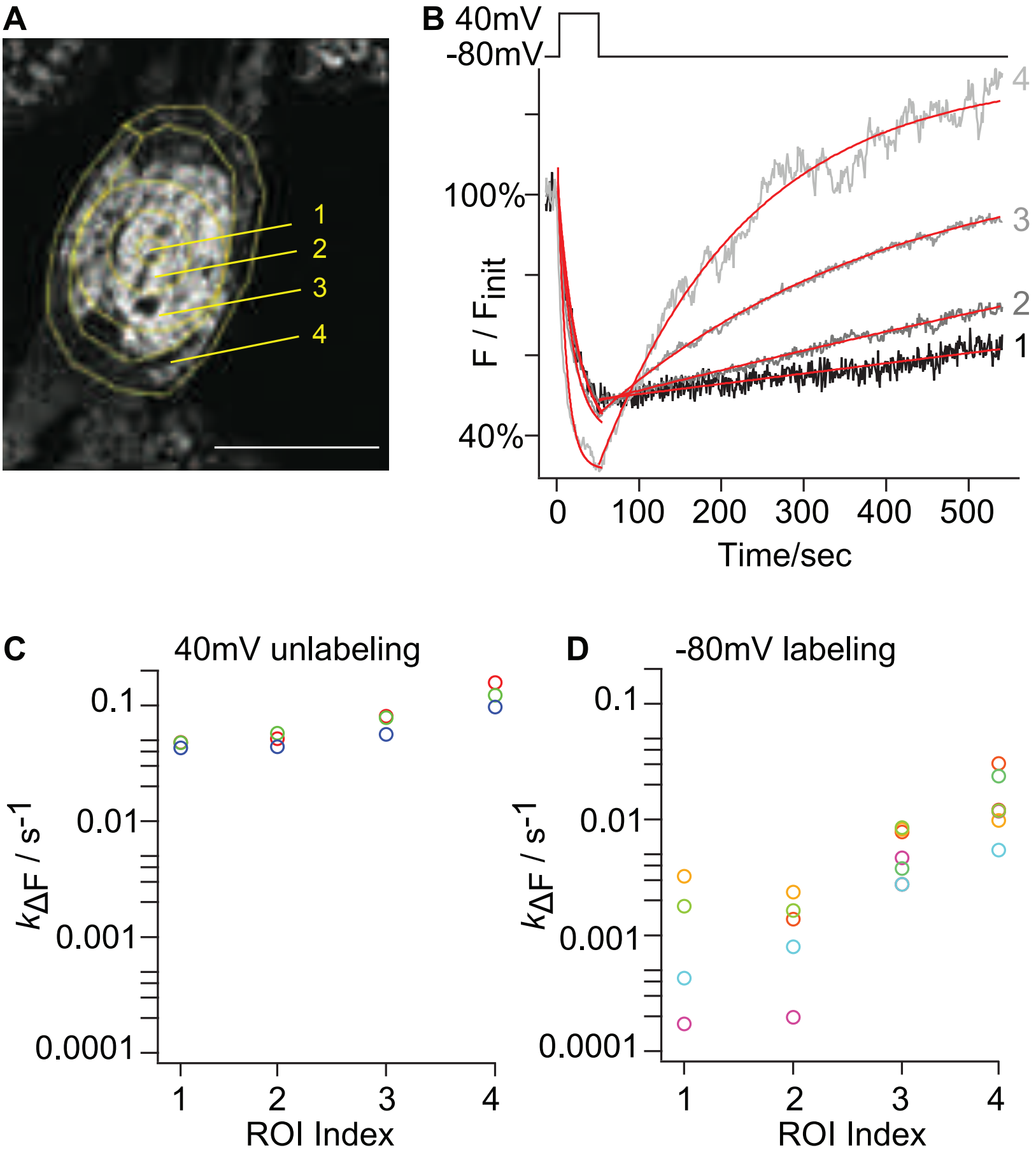

Figure 4 Supplement 2

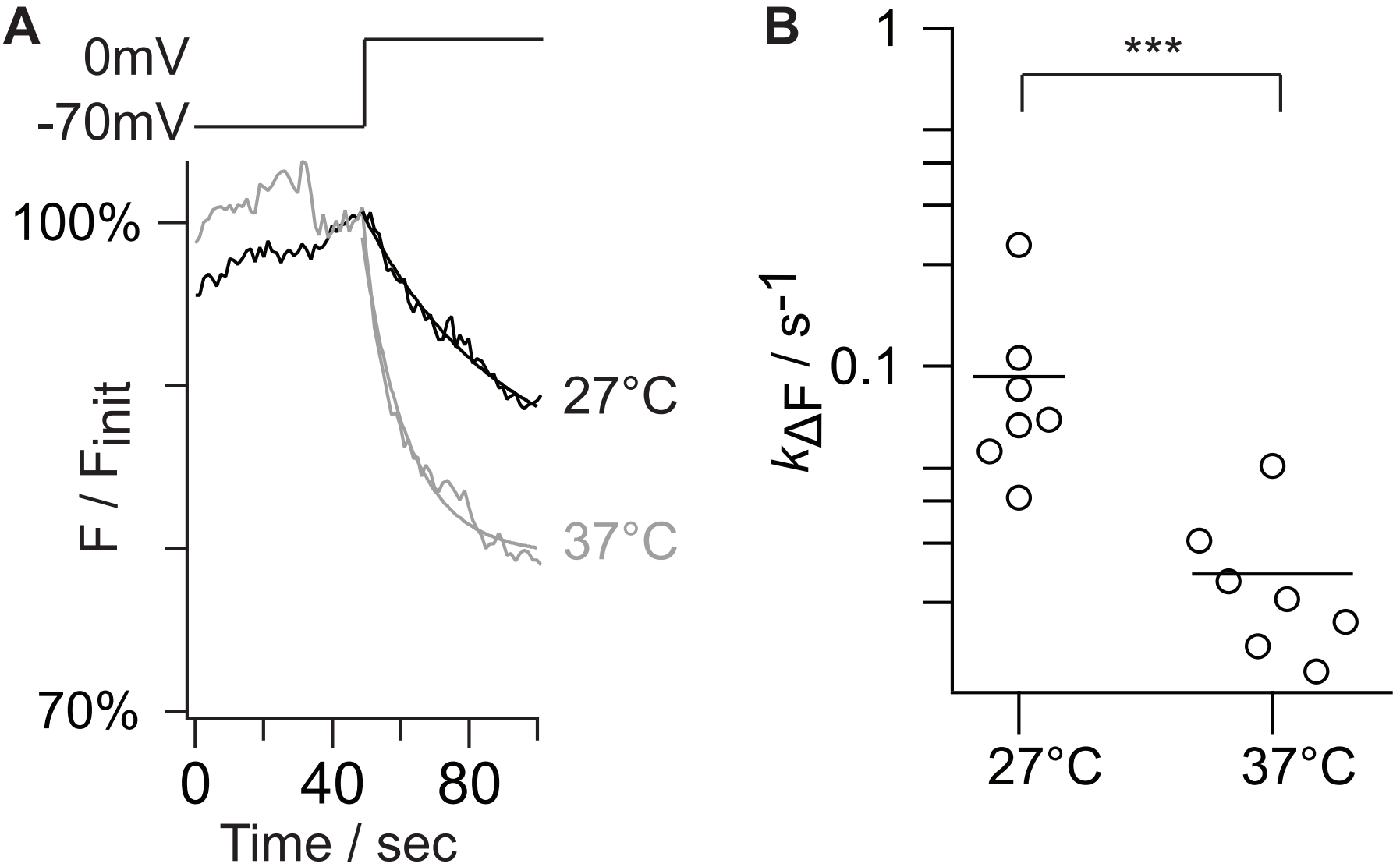

Figure 4

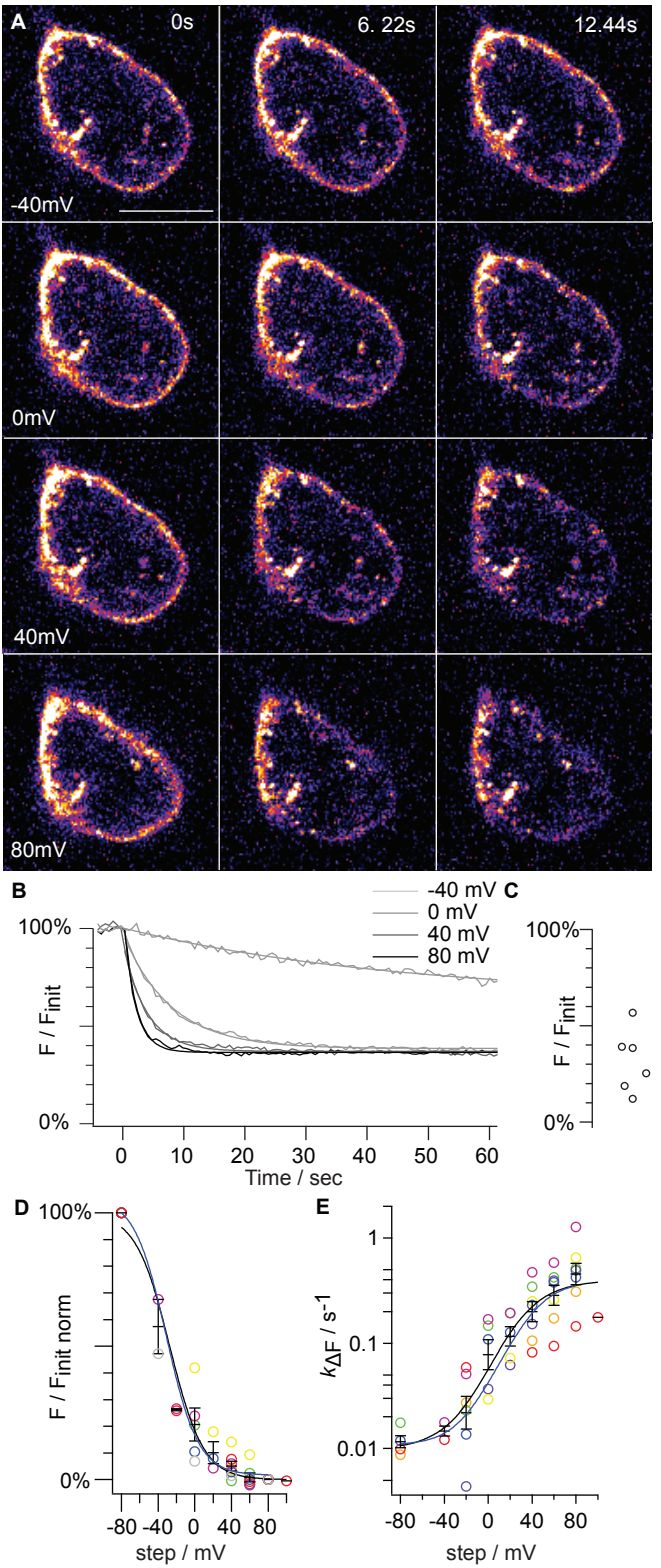
A
0s
6. 22s
12.44s
-40mV
0mV
40mV
80mV
B
-40 mV
0 mV
40 mV
80 mV
100%
0%
F / Finit
0
10
20
30
40
50
60
Time / sec
C
100%
0%
F / Finit
D
100%
0%
F / Finit norm
-80
-40
0
40
80
step / mV
E
1
0.1
0.01
kΔF / s-1
-80
-40
0
40
80
step / mV

Figure 5

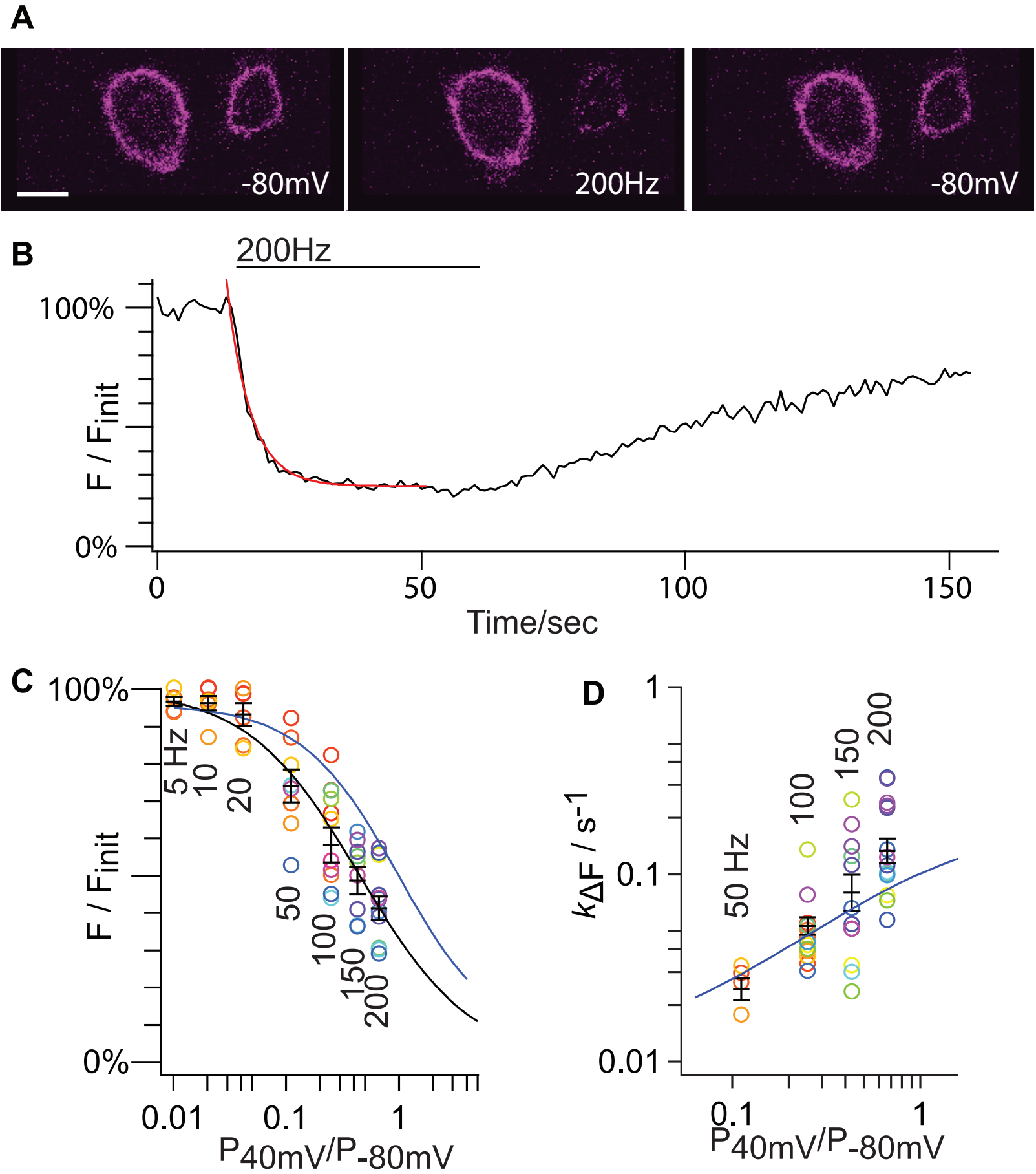
A
-80mV
200Hz
-80mV
B
200Hz
100%
0%
F / Finit
0
50
100
150
Time/sec
C
100%
0%
F / Finit
5 Hz
10
20
50
100
150
200
0.01
0.1
1
P40mV/P-80mV
D
1
0.1
0.01
kΔF / s-1
50 Hz
100
150
200
0.1
1
P40mV/P-80mV

Figure 6

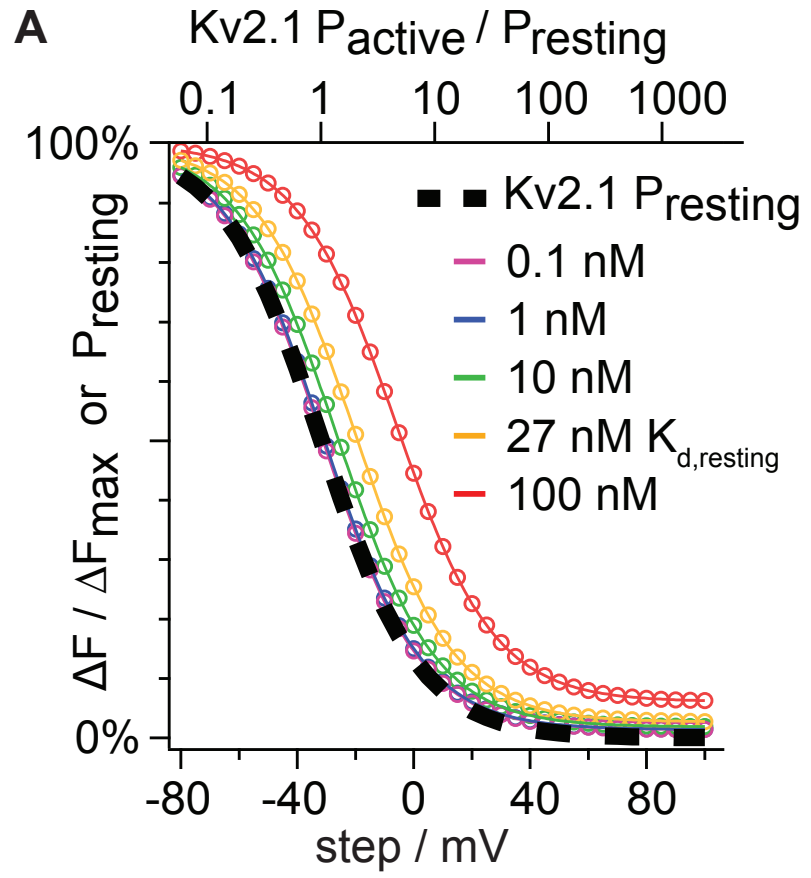
A
Kv2.1 Pactive / Presting
0.1
1
10
100
1000
100%
0%
ΔF / ΔFmax or Presting
Kv2.1 Presting
0.1 nM
1 nM
10 nM
27 nM Kd,resting
100 nM
-80
-40
0
40
80
step / mV

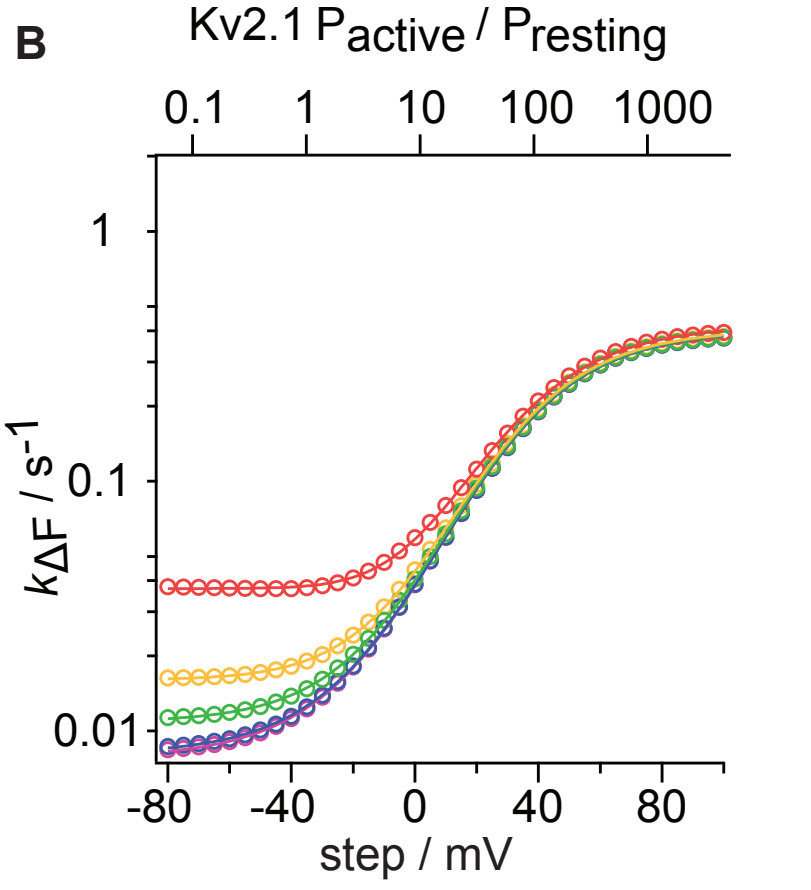
B
Kv2.1 Pactive / Presting
0.1
1
10
100
1000
1
0.1
0.01
kΔF / s-1
-80
-40
0
40
80
step / mV

Figure 7

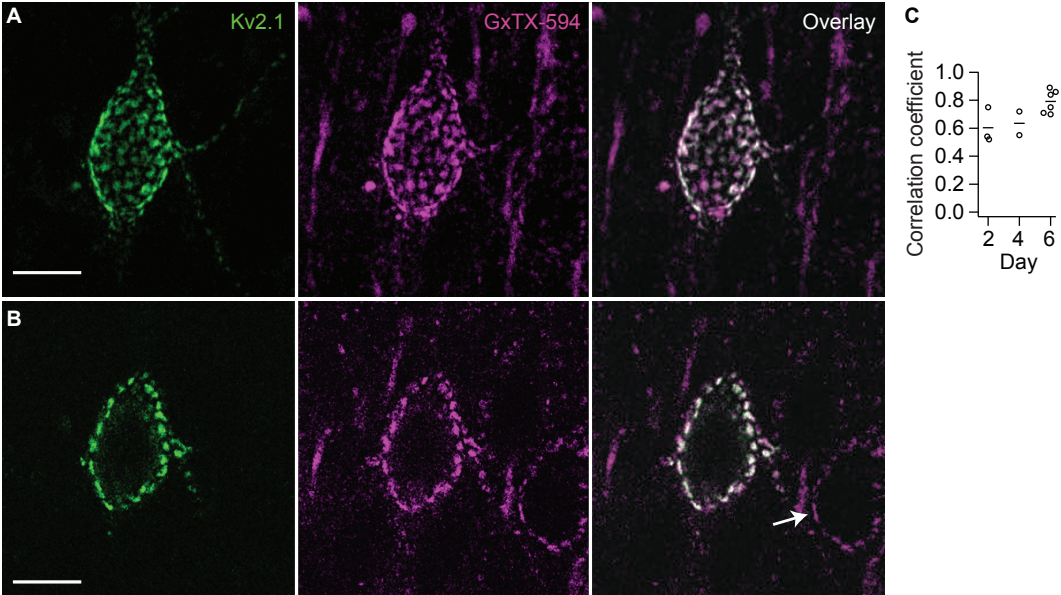
A
Kv2.1
GxTX-594
Overlay
B
C
Correlation coefficient
1.0
0.8
0.6
0.4
0.2
0.0
2
4
6
Day

Figure 7 Supplement 1

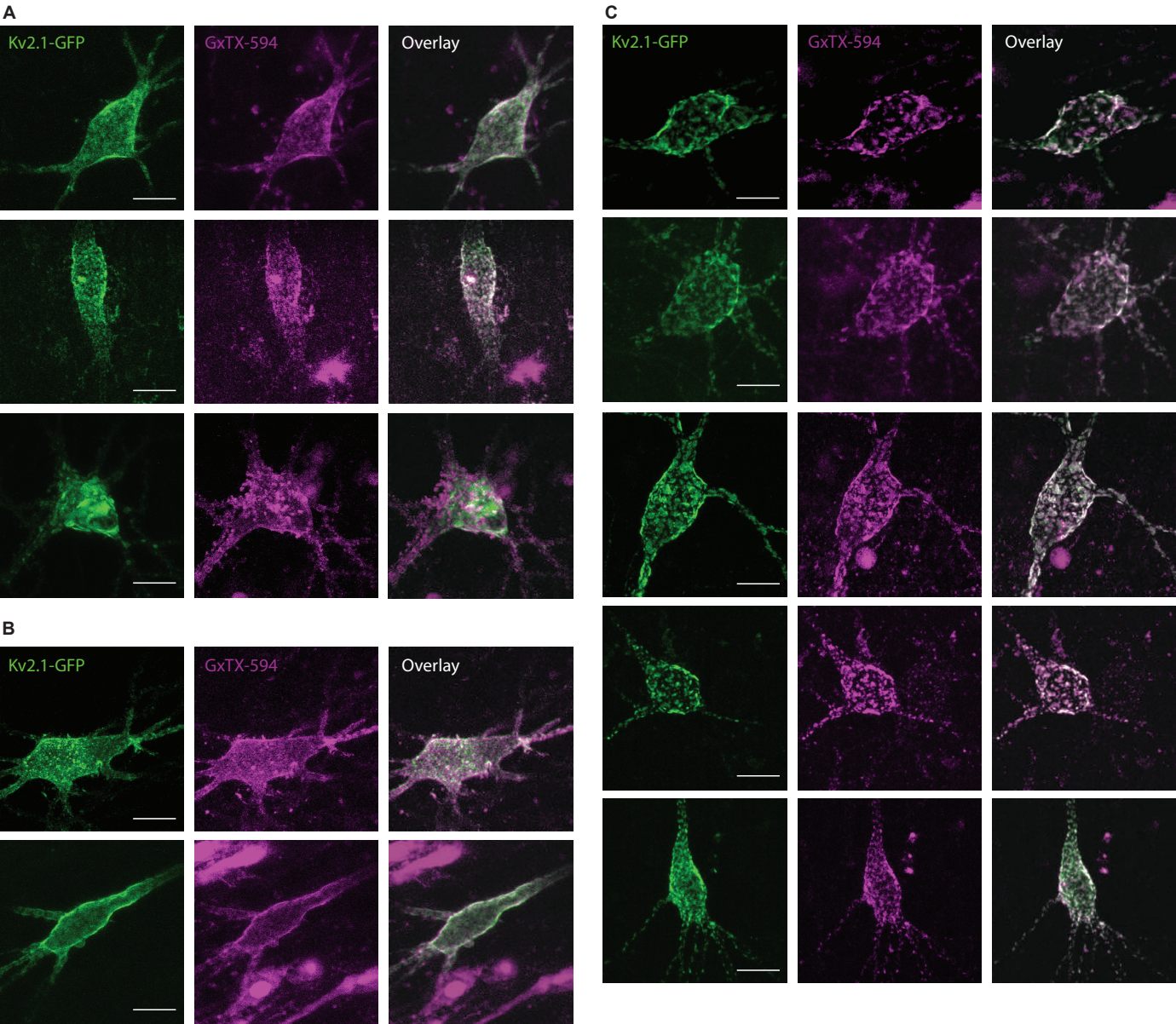

Figure 8

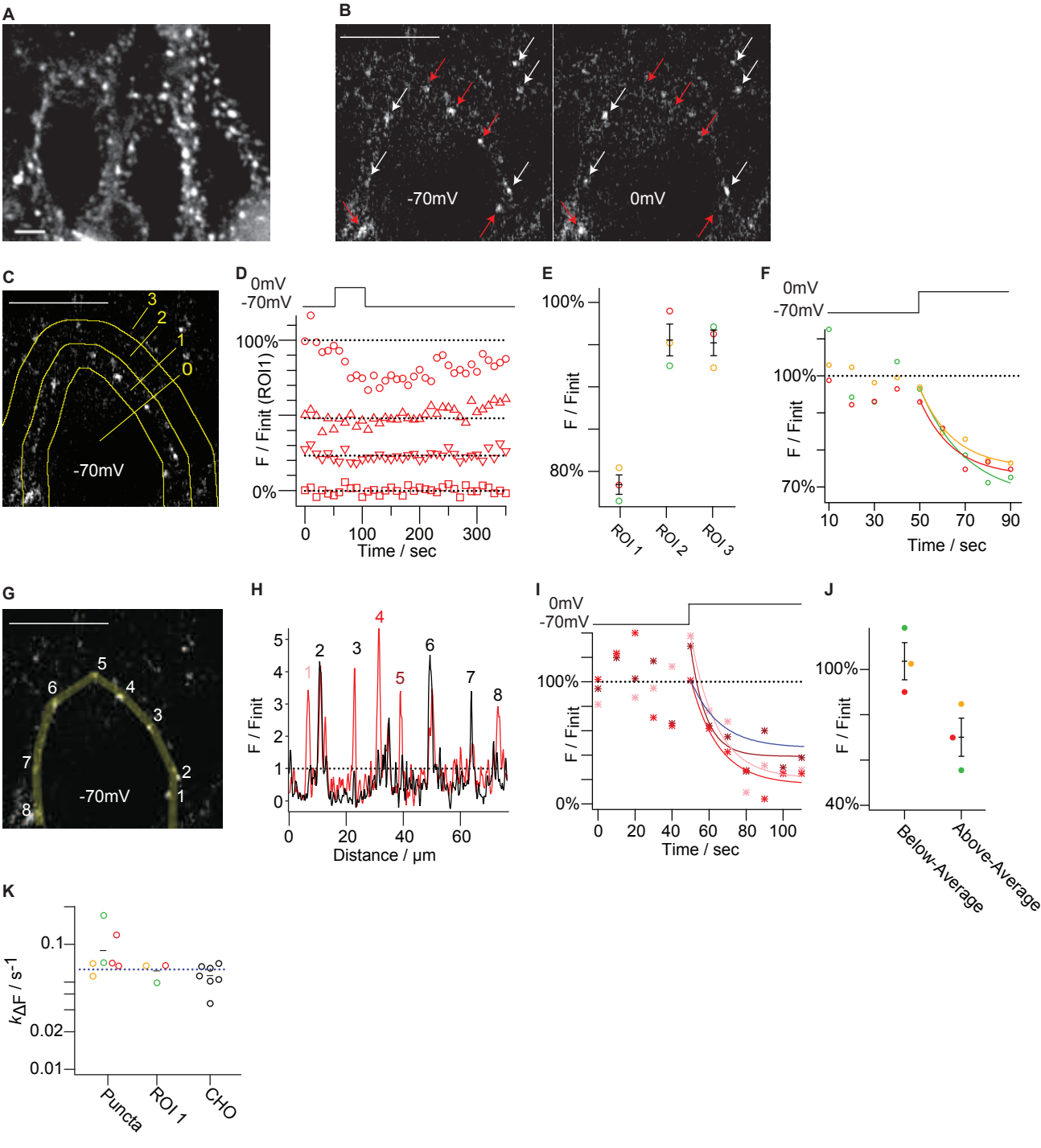
A
B
-70mV
0mV
C
3
2
1
0
-70mV
D
0mV
-70mV
100%
0%
F / Finit (ROI1)
0
100
200
300
Time / sec
E
100%
80%
F / Finit
ROI 1
ROI 2
ROI 3
F
0mV
-70mV
100%
70%
F / Finit
10
30
50
70
90
Time / sec
G
5
6
4
3
7
2
-70mV
1
8
H
1
2
3
4
5
6
7
8
F / Finit
0
20
40
60
Distance / µm
I
0mV
-70mV
100%
0%
F / Finit
0
20
40
60
80
100
Time / sec
J
100%
40%
F / Finit
Below-Average
Above-Average
K
0.1
0.02
0.01
$k_{\Delta F}$ / s$^{-1}$
Puncta
ROI 1
CHO